Atmos. Chem. Phys., 26, 9257–9275, 2026
https://doi.org/10.5194/acp-26-9257-2026

Atmospheric Chemistry and Physics
Open Access
EGU

Investigating information transfer in CO_2 flux inversions: an analysis of ensemble Kalman filter based on Monte Carlo simulations

Shidong Fan[1,2] **and Ying Li**[1,2,3]

[1]Department of Ocean Science and Engineering, Southern University of Science and Technology, Shenzhen 518055, China
[2]Center for the Oceanic and Atmospheric Science at SUSTech (COAST), Southern University of Science and Technology, Shenzhen 518055, China
[3]Southern Marine Science and Engineering Guangdong Laboratory (Guangzhou), Guangzhou, 511458, China

Correspondence: Ying Li (liy66@sustech.edu.cn)

Received: 2 February 2026 – Discussion started: 11 February 2026
Revised: 21 May 2026 – Accepted: 2 June 2026 – Published: 1 July 2026

Abstract. Top-down atmospheric CO_2 inversions are essential for estimating surface carbon fluxes, yet significant inter-system discrepancies highlight an incomplete understanding of how observational information is transferred to flux estimates. This study introduces a diagnostic strategy to explicitly investigate this information transfer, primarily in an Ensemble Kalman Filter (EnKF) system, with a comparative analysis of 4D-Var. Using Monte Carlo simulations, we analyze the spatial and temporal correlation patterns between CO_2 concentrations and fluxes, which play a crucial role in the inversion process by tracing information flow via the influence matrix. Our results reveal that these correlation scales are fundamentally set by the prescribed autocorrelation structure of the prior fluxes, rather than by atmospheric transport processes alone. We identify a resonance-like effect wherein correlated fluxes amplify concentration-flux correlations, while uncorrelated fluxes suppress them. The absence of this suppression for prescribed fluxes (e.g., anthropogenic emissions) can cause systematic signal misattribution. We further demonstrate that 4D-Var relies also heavily on flux autocorrelations due to its cost function's localized gradient. In both methods, the prior's critical role is mediated through the transitivity of strong autocorrelations. Simplified observing system simulation experiments corroborate these diagnostic findings: under the current sparse surface network in East Asia, a relatively longer correlation length (e.g., 600 km) is better than a short length (e.g., 100 km). This process-oriented perspective offers practically useful mechanistic insights for reconciling inversion results, optimizing observing networks, and strengthening carbon budget assessments.

1 Introduction

Anthropogenic emissions of greenhouse gases, most notably CO_2, are the principal driver of observed global warming (IPCC AR6, 2021). In response to the climate crisis, the accurate quantification of CO_2 sources and sinks has become paramount for informing mitigation strategies and tracking progress under international agreements. A variety of complementary approaches are used to estimate greenhouse gas fluxes, including bottom-up inventory methods, process-based ecosystem models, remote sensing products, and top-down atmospheric inversions (e.g., Piao et al., 2022). Bottom-up methods provide process attribution and sectoral detail, while top-down inversions provide an independent atmospheric constraint on the net surface–atmosphere exchange. Specifically, atmospheric inversion refers to the inference of surface fluxes from observed atmospheric CO_2 concentrations through atmospheric transport models and data assimilation frameworks. Its key strength lies in integrating atmospheric observations over large spatial scales, thereby offering information that is consistent with atmospheric concentration growth and complements bottom-up estimates (e.g., Chevallier, 2021). For this reason, atmospheric inversions have become a key pillar of major synthesis efforts such as the Global Carbon Budget (GCB), where they provide large-scale consistency checks and independent constraints on land and ocean carbon sinks (Friedlingstein et al., 2025).

Despite their growing application, CO_2 flux inversions still suffer from substantial uncertainty, which lead to significant discrepancies between inversion systems (e.g., Jin et al., 2023; Monteil et al., 2020). These uncertainties arise from various sources such as inaccuracies in transport models and poorly characterized prior covariance structures (Munassar et al., 2023; Schuh et al., 2022; Wang et al., 2020). Improving the reliability of inversion results requires a thorough understanding of these uncertainty sources. Recent intercomparison studies have quantified the relative contribution of these error sources to the final flux uncertainty (e.g., Chen et al., 2019; Munassar et al., 2023). For example, Chen et al. (2019) showed that uncertainty in atmospheric transport can result in a spread of CO_2 concentrations comparable to the spread induced by a 48 % uncertainty in natural fluxes. Similarly, Munassar et al. (2023) found that differences in transport models accounted for the majority of annual flux discrepancies in Europe, followed by the effects of boundary conditions and inversion schemes.

Among these uncertainty sources, the prior covariance structure plays a particularly fundamental role because it regulates how observational information is spatially and temporally propagated. A large body of inversion studies has explored different assumptions for constructing covariance matrices, including exponential or Gaussian correlation functions, anisotropic structures, biome-dependent formulations, and hyperparameters derived from flux residual statistics or synthetic experiments (e.g., Chen et al., 2023; Chevallier et al., 2012; Jacobson et al., 2023; Kountouris et al., 2018; Lauvaux et al., 2012; Niwa et al., 2022; Wesloh et al., 2024; Wu et al., 2013). These choices strongly influence the effective reach of sparse observations and therefore the posterior flux patterns. In general, shorter spatial correlation lengths tend to localize flux adjustments near observation sites, often preserving sharper spatial gradients but limiting the effective reach of sparse networks. In contrast, longer correlation lengths promote broader propagation of observational constraints, producing smoother posterior flux fields and often stronger large-scale regional adjustments (e.g., Lauvaux et al., 2012; Wu et al., 2013). In addition, biome-dependent correlation structures result in more reliable inversion results (e.g., Chen et al., 2023; Niwa et al., 2022).

Despite this extensive body of work on covariance specification, most previous studies have assessed these assumptions primarily through their impact on final posterior flux estimates or inversion performance metrics. By contrast, the internal statistical pathway through which prescribed covariance structures shape the propagation of observational constraints – before they manifest in posterior fluxes – remains insufficiently understood, leaving a mechanistic gap between covariance design choices and their practical inversion consequences. More specifically, it is unclear how information from sparse, pointwise concentration observations is transferred, transformed, and distributed across space and time to produce a flux field estimate, and what roles the prior covariance structures play in the "information transfer" process. This "information transfer" mechanism is the fundamental process by which an inversion system translates measurement into knowledge. Without a clearer understanding of this information pathway, it is challenging to optimally design systems, interpret differences among inversion systems, or diagnose why certain covariance assumptions improve or degrade posterior performance.

In this study, we address this gap by adopting a mechanism-diagnosing perspective aimed at making the internal statistical pathway of atmospheric inversion more transparent. Specifically, our objective is to reveal how prescribed prior covariance assumptions shape the propagation, spatial reach, and effective intensity of observational constraints before these effects emerge in posterior flux estimates. We achieve this by dissecting the core of the information transfer pathway from fluxes to observations within the Ensemble Kalman Filter (EnKF) framework, where the spatiotemporal correlation structure of the ensemble-derived Kalman gain governs how and where observational increments propagate to adjust prior fluxes. In such a framework, information transfer statistically refers to the propagation of observational increments to state variables via the prior covariance structure and Kalman gain. While a complete EnKF update integrates multiple factors (e.g., the observation-forecast innovation), this correlation structure exclusively determines the path and spatial extent through which observational constraints can reduce prior flux uncertainties.

The EnKF is uniquely suited for this diagnosis because it makes the mathematical kernel governing this assimilation pathway – the Kalman gain matrix (**K**, see Sect 2.1) – explicit and manipulable through an ensemble, which can be directly computed and analyzed via Monte Carlo simulation. Crucially, within this framework, the spatiotemporal autocorrelation structure, a foundational property of parts of **K** (dominating the spatiotemporal information pathway) that defines how uncertainties are presumed to correlate, can be systematically and flexibly manipulated through the generation of ensembles with prescribed core parameters (e.g., length scales and statistical distributions), and therefore enabling control over the resulting correlation structure in the Kalman gain. This approach allows us to directly test how the prescribed prior covariance structure fundamentally dominates and shapes the information transfer mechanism, offering a powerful and insightful perspective for analyzing data assimilation systems.

Therefore, we employ this controlled, large-ensemble EnKF approach to address the following key questions raised by theoretical and practical contradictions: (1) What determines the spatiotemporal scale and pattern of the ensemble correlations between concentrations and fluxes that drive the EnKF update? (2) How do the autocorrelation properties of prior fluxes, and the interactions between different flux components (e.g., anthropogenic vs. biospheric), modulate this information flow?

To provide broader context and highlight the generality of our findings regarding the role of prior covariance, we also present a comparative analysis with the four-dimensional variational (4D-Var) method. The equivalence between the Kalman filter update and the analytical solution of a 4D-Var problem under linear-Gaussian assumptions (Chevallier et al., 2005; Evensen et al., 2022) allows us to interpret our EnKF-based results in light of the 4D-Var formalism, where information transfer is mediated by the adjoint sensitivity and the prior covariance matrix. This comparison helps clarify how the fundamental constraint imposed by the prior covariance structure is a common determinant of information flow across different assimilation techniques.

The remainder of this paper is structured as follows: Sect. 2 details the methodological framework, including the ensemble configuration and the generation of prior perturbations. Section 3.1–3.2 presents results on the structure of concentration-flux correlations, and the factors influencing them. Section 3.3 provides a comparative perspective based on 4D-Var principles. Section 4 discusses the limitations of our approach. Section 5 summarizes the principal conclusions and their implications for future inversion studies.

2 Methods

2.1 A statistical derivation of the Kalman Filter for information transfer analysis

The core objective of this study is to diagnose how the a priori representation of uncertainty controls the assimilation of observational information into state estimates. We achieve this by introducing a perturbation-response strategy within the Ensemble Kalman Filter (EnKF) framework. The strategy is to design prior ensembles with distinct, prescribed statistical properties and then analyze how the resulting information pathways – encoded within the Kalman gain matrix – change in response.

There are several ways to derive the Kalman Filter, some of which rely on the normality assumption, while others do not (Tanizaki, 1996). We adopt the method that does not rely on the normality assumption in this work. More specifically, we employ traditional statistical estimation methods to derive the KF (Rao, 1994; Sengupta and Jammalamadaka, 2020). This approach seeks the optimal linear combination of prior and observational information that minimizes the analysis error variance while remaining unbiased, without presupposing any specific error distribution (Rao, 1994). The full derivation is provided in the Supplement (Sect. S1).

According to the linear estimation theory (Rao, 1994; Sengupta and Jammalamadaka, 2020), when observations and backgrounds are uncorrelated, the constrained best linear unbiased estimator (BLUE, linear estimator with minimum variance) of the general linear statistical model with constraint is

$$\hat{Z} = \mathbf{Z}^{\mathrm{b}} + \mathrm{Cov}\left(\mathbf{Z}^{\mathrm{b}}, \mathbf{P}\mathbf{Z}^{\mathrm{b}} - \boldsymbol{y}^{\mathrm{o}}\right)\left[\mathrm{Var}\left(\mathbf{P}\mathbf{Z}^{\mathrm{b}} - \boldsymbol{y}^{\mathrm{o}}\right)\right]^{-1} \left(\boldsymbol{y}^{\mathrm{o}} - \mathbf{P}\mathbf{Z}^{\mathrm{b}}\right) \tag{1}$$

where the state variable $\boldsymbol{Z} = \left(\boldsymbol{y}^{T}, \boldsymbol{E}_1^{T}, \ldots, \boldsymbol{E}_{\mathbf{k}}^{T}\right)^{T}$ is the vector of the modeled concentrations $\boldsymbol{y}$ and different fluxes $\boldsymbol{E}_i (i = 1, \cdots, k)$. $\mathbf{P}\mathbf{Z}^{\mathrm{b}} := \boldsymbol{y}^{\mathrm{b}} := H\left(M\left(\boldsymbol{y}_0, \boldsymbol{E}_1, \ldots, \boldsymbol{E}_{\mathbf{k}}\right)\right)$ is the vector of the modeled concentrations corresponding to the observed concentrations at specific locations and times. $\boldsymbol{y}^{\mathrm{o}}$ is the observation vector. M and H are the dynamical model (e.g., atmospheric transport model) and the observation operator, respectively, both of which need not to be linear.

Equation (1) can be simplified since the observation $\boldsymbol{y}^{\mathrm{o}}$ and the background $\mathbf{Z}^{\mathrm{b}}$ are uncorrelated (i.e., $\mathrm{Cov}\left(\boldsymbol{y}^{\mathrm{o}}, \mathbf{Z}^{\mathrm{b}}\right) = \mathbf{0}$):

$$\hat{Z} = \mathbf{Z}^{\mathrm{b}} + \mathrm{Cov}\left(\mathbf{Z}^{\mathrm{b}}, \boldsymbol{y}^{\mathrm{b}}\right)\left[\mathrm{Var}\left(\boldsymbol{y}^{\mathrm{b}}\right) + \mathrm{Var}\left(\boldsymbol{y}^{\mathrm{o}}\right)\right]^{-1} \left(\boldsymbol{y}^{\mathbf{o}} - \boldsymbol{y}^{\mathbf{b}}\right) \tag{2}$$

Furthermore, insert the covariance matrices $\mathbf{B}^{\mathrm{b}} := \mathrm{Var}\left(\mathbf{Z}^{\mathrm{b}}\right) = \mathrm{Cov}(\mathbf{Z}^{\mathrm{b}}, \mathbf{Z}^{\mathrm{b}})$ and $\mathbf{R} := \mathrm{Var}(\boldsymbol{y}^{\mathrm{o}})$, we have

$$\hat{Z} = \mathbf{Z}^{\mathrm{b}} + \mathbf{B}^{\mathrm{b}}\mathbf{P}^{T}\left(\mathbf{P}\mathbf{B}^{\mathrm{b}}\mathbf{P}^{T} + \mathbf{R}\right)^{-1}\left(\boldsymbol{y}^{\mathrm{o}} - \boldsymbol{y}^{\mathrm{b}}\right) \tag{3}$$

which is the widely used form of KF (where the projection $\mathbf{P}$ is usually replaced with a more general linear operator H) and in this form the equation can be treated as the analytical solution to the cost function of 4D-Var when the model and observation operator is linear (Evensen et al., 2022).

$$\mathbf{K} := \mathbf{B}^{\mathrm{b}}\mathbf{P}^{T}\left(\mathbf{P}\mathbf{B}^{\mathrm{b}}\mathbf{P}^{T} + \mathbf{R}\right)^{-1} = \mathrm{Cov}\left(\mathbf{Z}^{\mathrm{b}}, \boldsymbol{y}^{\mathrm{b}}\right) \left[\mathrm{Var}\left(\boldsymbol{y}^{\mathrm{b}}\right) + \mathrm{Var}\left(\boldsymbol{y}^{\mathrm{o}}\right)\right]^{-1} \tag{4}$$

is usually referred to the Kalman gain matrix and denoted by $\mathbf{K}$, while $\boldsymbol{y}^{\mathrm{o}} - \boldsymbol{y}^{\mathrm{b}}$ is known as the innovation vector (Asch et al., 2016). In the framework of EnKF and sequential assimilation, the covariances and variances in Eq. (4) can be easily evaluated using ensembles of fluxes and simulated concentrations.

Given the updated state variable, we can also update the covariance matrix:

$$\hat{B} = \mathrm{Var}\left(\hat{Z}\right) = \mathbf{B}^{\mathrm{b}} - \mathbf{B}^{\mathrm{b}}\mathbf{P}^{T}\left(\mathbf{P}\mathbf{B}^{\mathrm{b}}\mathbf{P}^{T} + \mathbf{R}\right)^{-1}\mathbf{P}\mathbf{B}^{\mathrm{b}} \tag{5}$$

In data assimilation literature, $\hat{Z}$ and $\hat{B}$ are generally written as $\mathbf{Z}^a$ and $\mathbf{B}^a$, where "a" stands for analysis.

In the Kalman gain equation, $\mathbf{B}^b\mathbf{P}^T$ (i.e., $\mathrm{Cov}\left(\mathbf{Z}^b, \boldsymbol{y}^b\right)$) is the primary signal or information transfer channel. It explicitly maps how uncertainties in specific state variables (e.g., fluxes in a given region) covary with projected observations. Its spatial pattern directly determines the pathways and directions in which observational information propagates to update the state. Therefore, in this study, we adopt a perturbation-response strategy. By designing prior ensembles to systematically alter $\mathbf{B}^b$ and observing the consequential changes in the ensemble-based $\mathbf{B}^b\mathbf{P}^T$ to probe the sensitivity of the system's core information-transfer physics. To be consistent with most literature, we will use $\mathbf{H}$ instead of $\mathbf{P}$ in the following.

2.2 Transport model and experiment implementation

We implement this strategy through a series of high-resolution Monte Carlo simulations using the Weather Research and Forecasting model coupled with the Vegetation Photosynthesis and Respiration Model (WRF-VPRM, version 3.9.1.1). WRF-VPRM integrates the diagnostic VPRM biosphere model into WRF-Chem. VPRM parameterizes biospheric CO_2 fluxes – gross ecosystem exchange (GEE) and ecosystem respiration (RES) – as functions of satellite-derived vegetation indices and meteorological drivers (Ahmadov et al., 2007; Beck et al., 2011; Mahadevan et al., 2008). We extended the standard VPRM formulation by adding five parameters per vegetation type (63 total across seven major types) to better represent the nonlinear environmental response of respiration, following Gourdji et al. (2022). Default parameter values were drawn from established literature (Dong et al., 2021; Gourdji et al., 2022; Li et al., 2020; Raju et al., 2023), with minor adjustments. The model domain covered East Asia at a 27-km horizontal resolution with 39 vertical levels (Fig. S1). All ensemble members were driven by identical meteorological fields, constrained by NCEP GDAS/FNL 0.25° analysis data with observation nudging. The planetary boundary layer scheme for vertical mixing was the Asymmetric Convective Model, version 2 (ACM2, Pleim, 2007). Additional WRF model configurations are available in our previous publications (e.g., Fan et al., 2021; Fan and Li, 2022, 2023; Gao et al., 2022; Li and Li, 2023). To capture distinct seasonal regimes, base simulations were conducted for two-week periods in January and July 2016. Due to the high computational cost of the 500-member ensemble, shorter one-week simulations were used for specific sensitivity tests (Super et al., 2020).

All experiments use a 500-member ensemble and are driven by identical meteorological fields to isolate the impact of flux uncertainty. The core of the experimental design lies in manipulating the representation of biosphere flux uncertainty, as shown in Table 1. The OFF600 case serves as the baseline, employing offline perturbations with a 600 km spatial correlation. The ONLINE case generates uncertainty by perturbing ecological model parameters (producing process-driven covariance with longer correlation length scales), while the OFF100 case uses offline perturbations with a shorter correlation length (100 km). The three experimental cases are designed with two primary objectives. First, they systematically vary the spatial correlation length scales of the biospheric flux perturbations (e.g., 100 km vs. 600 km) to examine how the assumed correlation scale influences the resulting concentration–flux relationships and information transfer pathways. Second, the ONLINE case generates flux uncertainty through perturbations of VPRM parameters, producing a spatial autocorrelation structure that is linked to land-cover types. This allows us to assess not only the effect of correlation length scale but also the influence of the spatial structure (shape) of the autocorrelation. Anthropogenic and ocean fluxes are perturbed consistently across all cases (see Sect. 2.3). Perturbations are applied to all three flux components in order to investigate the interactions among co-existing uncertain fluxes, which are central to the analysis of signal "dilution" discussed later.

2.3 Generation of ensemble inputs

The utility of Monte Carlo simulations for understanding the EnKF method has been demonstrated in simple experiments by Chen et al. (2019) and explored more extensively in other domain research fields (Miyoshi et al., 2014). In this study, we extend this approach to analyze the nature of concentration-flux correlations, which play a central role in information transfer. We investigate their general characteristics in space and time and identify key influencing factors such as flux autocorrelations (which relate to the background covariance matrix) and the interactions between uncorrelated flux components (e.g., anthropogenic and biospheric fluxes).

To run Monte Carlo simulations, proper input ensembles must be generated before the run. For regional CO_2 transport simulations, the primary inputs (aside from meteorological fields) are CO_2 fluxes, initial concentrations (IC), and lateral boundary conditions (BC). We will investigate the impacts of BC in another work. Accordingly, ensembles were constructed for both fluxes and IC. A critical design element in ensemble generation for CO_2 flux inversion is the characterization of spatiotemporal correlation structures. There is limited discussion in the literature regarding the spatial correlation of IC; we thus followed the approach of Miyoshi et al. (2014) by using CO_2 fields at different time steps from an independent simulation to represent different ensemble members. The independent simulation uses another transport model (Community Multiscale Air Quality model, CMAQ, version 5.4) with CO_2 fluxes that differ from those employed in the Monte Carlo simulations.

For anthropogenic emissions over land that are spatially regridded and temporally allocated from the monthly EDGAR-GHG (v6.0) using the corresponding high reso-

Table 1. Case design of this study.

Case		Flux origin	Perturbation correlation function	Perturbation standard deviation
OFF600 (BASE)	F_{BIO}	Mean of the ONLINE ensembles	Space and time exponential functions and 600 km, 1 month correlation lengths	40 % of mean
	F_{ANT}	EDGAR-GHG v6.0	The same as F_{BIO}	
	F_{OCE}	Online calculated using monthly pCO_2 and modeled concentrations and so on.	pCO_2 perturbed with a space exponential function and a 1000 km correlation length.	
ONLINE	F_{BIO}	Online calculated using an ensemble of VPRM parameters	VPRM parameters independently perturbed.	40 % of mean
	F_{ANT}	The same as OFF600	The same as OFF600	
	F_{OCE}	The same as OFF600	The same as OFF600	
OFF100	F_{XXX}	The same as OFF600 but with 100 km space correlation length of F_{BIO}		

Note: XXX in F_{XXX} represents ANT, BIO, or OCE.

lution temporal profiles (Janssens-Maenhout et al., 2019; Crippa et al., 2020), we implemented a simple space-time correlation function, characterized by an exponential function with correlation lengths of 600 km (following Ma et al. (2019) for other anthropogenic emission species) and 1 month (considering the time resolution in the emission inventory), see Fig. S2 for an example of the correlation functions. An ensemble of Gaussian fields with a standard deviation of 40 % was generated based on this space-time correlation function using a Python toolbox GStools (Müller et al., 2022).

Specifically, the spatial covariance between two grid cells i and j separated by distance d_{ij} is modeled as:

$$\mathbf{B}_{ij} = \sigma_i \sigma_j \cdot \exp\left(-\frac{d_{ij}}{L}\right)$$

where σ_i and σ_j are the prior uncertainty standard deviations (set to 40 % of the mean flux), and L is the spatial correlation length (600 km for the baseline OFF600 case, 100 km for OFF100, and spatially variable for ONLINE). This exponential correlation function is chosen for its mathematical simplicity and widespread use in regional inversion systems (e.g., Lauvaux et al., 2012; Wu et al., 2013). For biospheric fluxes, the ONLINE case utilized online-calculated fluxes derived from an ensemble of VPRM parameters. This approach is conceptually similar to that of Super et al. (2020) , who applied ensemble methods to fossil fuel emissions. The ensemble of VPRM parameters is generated independently by drawing from a normal distribution with averages the same as some reported values in previous studies (see Sect. 2.2) and a standard deviation of 40 %. The ensemble means of GEE and RES from these simulations were subsequently used as the baseline fluxes for the OFF600 case. To generate two ensembles for OFF600, these mean GEE and RES were perturbed using the same method as that applied to anthropogenic emissions.

For oceanic fluxes, we implemented a module to calculate the fluxes online using the monthly surface ocean partial pressure of CO_2 (pCO_2) (Fay et al., 2021), the modeled atmospheric CO_2 concertation, and the parameterized gas transfer velocity (Wanninkhof, 2014). This is similar to the biospheric fluxes in the sense of online calculation, but the oceanic fluxes rely more on the atmospheric and oceanic concentrations and may have different correlation structures compared to biospheric fluxes. The monthly pCO_2 was perturbed using GStools with a space exponential correlation function that has a correlation length of 1000 km. The standard deviation of the perturbation was also 40 %, as is the case with other fluxes.

2.4 Diagnostic analysis and choice of observation sites

The core diagnostic metric is the ensemble sample correlation between simulated concentrations at observation points and prior fluxes across the entire spatiotemporal domain. These correlation patterns directly estimate the influence functions within the Kalman gain $\mathbf{K}$, thereby mapping the information transfer pathways under a given prior $\mathbf{B}$.

For diagnostic analysis of concentration-flux response, we need to set up observation sites. For surface CO_2, we choose the GAW sites within our domain (Global Atmosphere Watch Station Information System, 2024) and some additional sites in China. For satellite XCO_2, we select multiple locations somewhat arbitrarily along the OCO2 track over land and are also denoted as “sites” for convenience (OCO-2/OCO-3 Science Team et al., 2024). The locations of the 111 CO_2

sites and the 41 XCO_2 sites are shown in Fig. S3. For further spatial illustration, we select 26 CO_2 sites with available data at some time (World Data Centre for Greenhouse Gases, 2025), excluding two sites in Japan that are too close to others, leaving 24 sites. Similarly, we select 24 sites from the 41 XCO_2 sites for further illustration. Only half of the 24 sites are shown in the main text when illustrating the correlation patterns, while the others are included in the SI when necessary.

Since our simulations in different months are relatively short, we need to check IC's influence first. The autocorrelation of modeled CO_2 at a site with IC at the same site decreases rapidly, and this reduces is relatively homogeneous in space, except for some sites occasionally (Fig. S4). Therefore, a one- or two-week simulation can be used to explore the transport behavior of ensemble fluxes. In addition, our modeled F_{BIO}, F_{OCE}, surface CO_2, and XCO_2 are not far from widely used results (Fig. S5), demonstrating the relevance of our simulations to real applications.

3 Results and discussions

3.1 Spatial structures of concentration-flux correlations

3.1.1 Spatial patterns of correlations

In EnKF-based CO_2 inversion systems, the information from observations is primarily transferred through correlations between observed concentrations and unobserved fluxes. At the same time, atmospheric transport, as well as the assumed uncertainties in both fluxes and observations, also play fundamental roles by shaping the uncertainty of modeled concentrations and the resulting observational influence. In the present study, we specifically focus on the spatial extent of observational constraints on fluxes. Thus, analyzing the correlation structures between CO_2 concentrations and fluxes is essential. For notational convenience, we occasionally use M to denote CO_2 concentration in the following, with the subscript TOT indicating total concentration, as distinct from individual tracers such as ANT, BIO, and OCE. To illustrate the typical spatial influence of fluxes, we compute the correlation between the prior flux state at the initial time and the resulting ensemble concentrations after one week of transport (at hour 168). This choice partially reflects the sequential update logic of an EnKF (Houtekamer and Mitchell, 2001), where observations constrain fluxes within a time window one by one. While this provides a representative snapshot, the correlation structures are qualitatively similar at other times (temporal evolution is analyzed in Sect. 3.2). This study uses results from 500-member simulations to characterize these correlation structures while results with smaller ensemble sizes are exemplified in Fig. S6.

In the 500-member simulations, the spatial correlation patterns are demonstrated, showing large values near the observation sites and minimal noise-like values (i.e., randomly mixed positive and negative values) in remote areas if the sites are influenced by a specific flux (Figs. 1 and S7). For example, in January, the LAN, HAT, and WLG sites exhibit strong correlations between surface M_{TOT} and nearby F_{ANT} (Fig. 1b), F_{OCE} (Fig. 1c), and F_{BIO} (Fig. 1d), respectively. Similarly, in July, the SDZ, HAT, and WLG sites exhibit strong correlations (Figs. S7Co, 1i, and 1j). Many other sites also show significant correlations, suggesting the feasibility of using surface M_{TOT} observations to invert fluxes. In general, the correlation between surface M_{TOT} and nearby F_{ANT} is more potent in winter (January) than in summer (July), with notable correlations primarily observed in the eastern China, Korea, and Japan (Figs. S7A and C), where the F_{ANT} is large and concentrated. In contrast, the influence of F_{BIO} is more pronounced in the western region, with strong correlations present in both winter and summer (Figs. S7E and G). At island sites, the influence of F_{OCE} can be significant, especially in summer when the monsoon is directed landward. The specific spatial morphology of correlations at individual sites – such as their asymmetry and elongation direction – clearly reflects the modulating influence of local atmospheric transport processes.

Conversely, the overall spatial correlations pattern exhibits a relatively regular distribution, showing maximum values near the sites and a stable decline with distance. The locations of the strongest correlations are typically at or near the observation sites, mainly downwind of the monsoon directions. However, some sites exhibit "remote" correlations for surface M_{TOT} (e.g., Figs. S7Ah and Bo). One notable characteristic of the spatial patterns is that the values are monotonic, which has an important implication. Observation at specific site can only influence a neighborhood's fluxes by increasing or decreasing them overall. In contrast, prior fluxes in this neighborhood may exceed the true values in some locations while falling short in others. Therefore, only a sufficient combination of observations can potentially recover the true fluxes from the prior estimates by both increasing and decreasing the fluxes across the neighborhood.

Regarding the measurement heights, the correlation patterns between M_{TOT} at different heights, including XCO_2, and fluxes are generally consistent with those derived from surface M_{TOT} (compare Figs. 1 and S8). This strong similarity implies that, in terms of diagnosing the information transfer pathway, the flux signals captured by higher-altitude M_{TOT} or XCO_2 are dominated by similar source regions as the surface M_{TOT}. Given the similarity of the correlation patterns across observation heights, the following analysis focuses primarily on surface concentrations. However, it should be emphasized that the difference in the observation innovations and transport errors can affect the relative influence of surface M_{TOT} versus higher-altitude M_{TOT} or XCO_2 in the inversion.

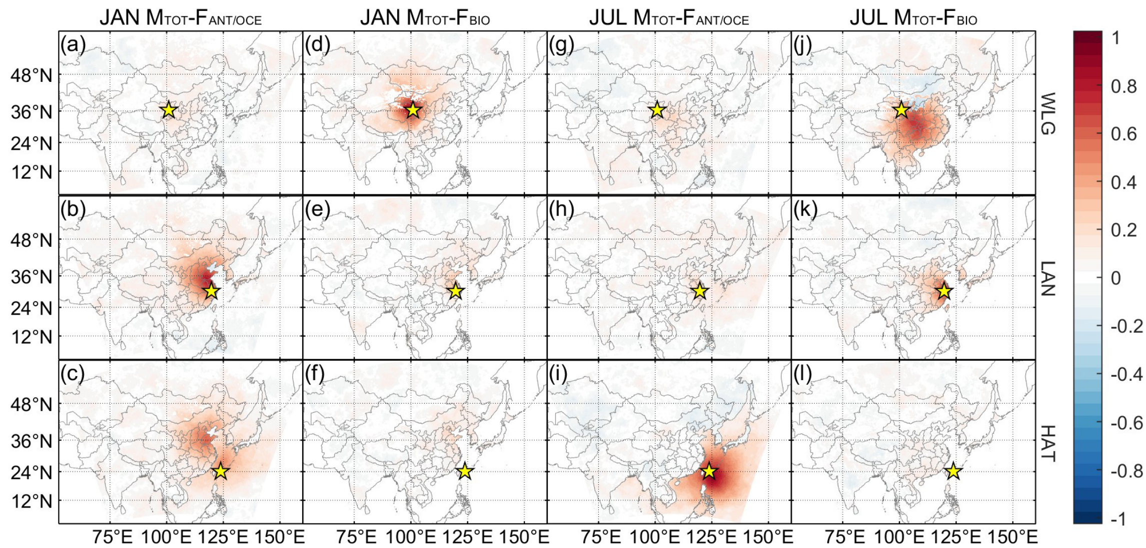

Figure 1. Spatial patterns of 500-member correlations between the 168th-h M_{TOT} at sites and the 0th-h fluxes (F_{ANT}, F_{OCE}, and F_{BIO}) across the domain. Each row represents a site, labeled at right. **(a–c)** M_{TOT}-F_{ANT} and M_{TOT}-F_{OCE} in January; **(d–f)** M_{TOT}-F_{BIO} in January; **(g–l)** July.

3.1.2 The influence of flux autocorrelations on the spatial correlation patterns

The spatial pattern of concentration-flux correlations is statistically similar to that of flux autocorrelation (compare Figs. 1d and S2a), which shows a clear decline with distance. Although the specific shapes of correlations vary across sites, the average decay scale of their spatial influence seems aligns closely with the autocorrelation length of the prior fluxes. For instance, the strong correlation areas for M_{TOT}-F_{OCE} are larger than those for M_{TOT}-F_{ANT} or M_{TOT}-F_{BIO}, consistent with its longer autocorrelation length 1000 km of F_{OCE} than the 600 km of the other fluxes (e.g., compare Fig. S7Cp and Dc). To further prove this, we introduce two additional simulation cases: ONLINE, which utilizes an online perturbed F_{BIO} with land-cover-based autocorrelation patterns and has longer correlation length scales, and OFF100, which employs a shorter spatial correlation length of 100 km (see Table 1). Figure 2 illustrates the spatial correlations between surface M_{TOT} and F_{BIO} for these two cases, which can be compared to Figs. 1d–f and j–l for the OFF600 case.

As expected, the ONLINE case exhibits longer correlation scales in space than the OFF600 case, and the spatial patterns of correlations are predominantly influenced by land cover. Similarly, the OFF100 case shows a shorter correlation scale than the OFF600 case, consistent with the 100 km correlation length. These two additional cases clearly illustrate that the autocorrelation lengths of fluxes largely determine the basic spatial patterns of the concentration-flux correlations, despite that transport processes may translate the high-value areas and deform the shapes of the patterns to some extent. This property provides a more precise explanation of why the autocorrelation scales of the fluxes are critical in flux inversion, as CarbonTracker identifies them as one of the two primary "tuning knobs" (Jacobson et al., 2023). This is because these scales determine the possible spatiotemporal extent to which a concentration observation can contribute to inverting the fluxes.

In addition to the scale of correlation, the strength of the correlation between concentrations and fluxes is also influenced by the autocorrelation length of the fluxes. Notably, both the correlation scale and strength diminish simultaneously in the OFF100 case compared to the OFF600 case (e.g., compare Figs. 1j and 2j). Moreover, the correlation strength in the ONLINE case is greater than in the OFF600 case. This weaker correlation in cases with shorter correlation lengths for fluxes and a stronger correlation in cases with more considerable correlation lengths suggests a form of "resonance" of fluxes at different locations during transport, enhancing the maximum correlations observed. This "resonance" effect essentially stems from the integrative amplification of spatially and temporally coherent signals, which is also enabled by strong autocorrelations, by atmospheric transport. More technically, the effect reflects the constructive aggregation of contributions from spatially correlated flux perturbations to the modeled concentration response, such that concentration-flux covariance structures align more effectively with the transport-induced sensitivity pattern. When fluxes are strongly positively correlated over a large region (i.e., have a long autocorrelation lengths), the CO_2 signals released from these areas exhibit similar phases and variation trends during transport. Integrated by atmospheric flow and arriving at the observation site, their contributed concentration fluctuations add up coherently, thereby producing

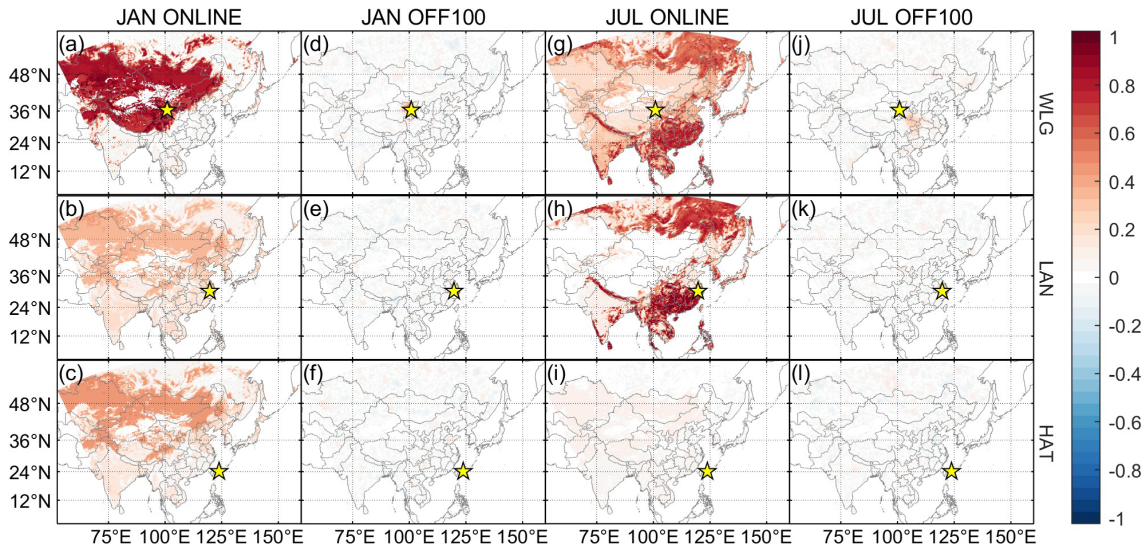

Figure 2. Spatial patterns of the M_{TOT}-F_{BIO} correlations in different cases. Each row represents a site, labeled at right. **(a–c)** ONLINE in January; **(d–f)** OFF100 in January; **(g–l)** July.

a stronger concentration-flux correlation. Conversely, if the spatial correlation scale of the fluxes is short, the emission signals from different upwind grid cells are independent of each other and randomly cancel out, resulting in a weak net signal at the site and consequently a lower correlation.

These two effects, directly or indirectly imposed by flux autocorrelations, make it more challenging to configure the space–time autocorrelation functions of fluxes (i.e., to specify the prior covariance matrix **B**). While data-driven methods that construct correlation functions directly from observations tend to yield shorter (i.e., < 100 km) spatial correlation lengths (Kountouris et al., 2015, 2018) in Europe, our results indicate that a shorter correlation length not only reduces the correlation scale but also weakens the correlation strength, further amplifying the limitations of sparse observations.

Therefore, in the context of sparse surface observations, it is not recommended to strictly follow suggestions that advocate very short spatial autocorrelation lengths (e.g., 100 km). This issue is more clearly illustrated in Fig. 3, which shows the sum of localized (Gaspari and Cohn, 1999) concentration–flux correlations across all the 24 sites. When a spatial autocorrelation length of 600 km is used, the summed correlations cover most of the domain except South Asia and some weak-flux regions (Figs. 3a and c), indicating that fluxes over most regions can be constrained by observations from these 24 sites. In contrast, using a much shorter spatial autocorrelation length results in extensive blank areas, indicating that fluxes over most regions cannot be effectively constrained by these observations (Figs. 3b and d).

Consequently, for many applications it may be reasonable not to strictly follow observation-derived correlation lengths, but instead to adopt longer ones (e.g., Chandra et al., 2022; van der Laan-Luijkx et al., 2017).This study demonstrates that, for the current sparse surface observation network in East Asia, adopting a flux spatial autocorrelation length of approximately 600 km is appropriate. It is important to clarify that this length scale is not directly "measured" from the observations but rather serves as a parametric representation based on the physical understanding of flux spatial continuity in the region. The specification of the spatial correlation length L in the prior covariance matrix **B** serves two distinct purposes. The first is to represent the assumed spatial structure of flux errors. The second, related to the first and revealed by our results, is to regulate the propagation of observational information. Under a sparse observation network, the latter can become the dominant constraint. Mathematically, in the Kalman gain expression $\mathbf{K} = \mathbf{B}\mathbf{H}^T(\mathbf{H}\mathbf{B}\mathbf{H}^T + \mathbf{R})^{-1}$, the term $\mathbf{B}\mathbf{H}^T$ governs how observational increments propagate to state variables. Even when atmospheric transport (**H**) physically links distant locations, prescribing a short correlation length (e.g., 100 km) forces the prior covariances to near zero for separations beyond approximately 300 km. This mathematical cutoff is independent of transport; the Kalman gain simply has no pathway to connect the observation to that distant flux, regardless of how well the transport model represents the physical connection. Here, it is important to distinguish between two aspects of concentration–flux correlations: the location of the correlation maximum (determined by atmospheric transport) and the spatial extent of the high-correlation region (determined by the prescribed autocorrelation length L). Even with a short L, transport can shift the correlation maximum far from the flux source. However, a short L causes the high-correlation region to be narrow, so that sparse observations can only constrain a small area around the location with strongest correlation. A longer

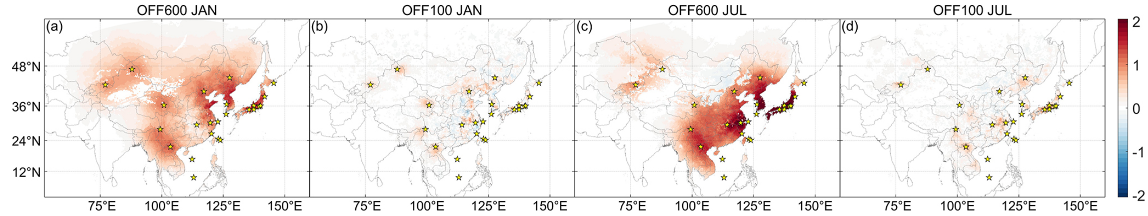

Figure 3. Composite observational influence extent for the different experimental configurations, represented by the summation of the M_{TOT}–F_{BIO} correlations. **(a)** OFF600 in January, **(b)** OFF600 in January, **(c–d)** July.

L broadens the high-correlation region, enabling the same sparse network to constrain a much wider domain, as shown in Fig. 3. Thus, the recommended 600 km length is not a claim about the true spatial scale of flux errors, but a mathematical requirement to keep the information pathway open under sparse observations, allowing the inversion to utilize the longrange information that transport physically provides.

Denser XCO_2 observations may alleviate the limitations on autocorrelation length scales imposed by surface observation sparsity; however, the spatiotemporal sampling of XCO_2 is irregular, and its information "content" is generally lower than that of surface M_{TOT} observations. It therefore remains unclear to what extent these limitations can be mitigated. Nevertheless, when only surface M_{TOT} observations are used, the flux autocorrelation length should not be too short. In the future, as observational density increases, this optimal scale may change, which could enable more details spatial pattern of the inversion.

To provide a consistency check of the diagnostic results regarding the correlation length, we further performed a set of simplified inversion experiments within an observing system simulation experiments (OSSE) framework (see Sect. S2 in the Supplement). Although not designed as a comprehensive evaluation of inversion performance, these experiments show (Fig. S9) that when only sparse surface observations are used, a short spatial autocorrelation length (100 km) leads to minimal and highly localized posterior adjustments, whereas a longer length scale (600 km) enables broader propagation of observational constraints and improves agreement with the true flux. The inclusion of satellite observations increases overall constraint, but does not fully compensate for overly short correlation lengths. These results are consistent with the mechanism-diagnostic findings presented above.

In addition to the characteristic correlation length scale, the form of the prescribed correlation function (e.g., Gaussian, exponential, and hyperbolic) also influences how observational constraints propagate. In principle, correlation functions with longer tails can extend the theoretical reach of observational influence to more remote fluxes. However, our sensitivity tests (Fig. S10) show that this extension is limited in practical EnKF applications. Although slowly decaying functions increase weak long-range correlations, the resulting concentration–flux correlations at remote distances rapidly decrease to values that are difficult to distinguish from ensemble sampling noise. At the same time, the longer tail redistributes the correlation structure and tends to weaken nearby correlations, where observational signals are strongest and most robust. Therefore, the choice of correlation-function shape involves a practical trade-off between slightly increasing the theoretical adjustment range and preserving strong local constraints.

More broadly, similar to the choice of a longer correlation length, this trade-off reflects a balance between physical realism and inversion efficiency. Ideally, prior correlation functions (including their shape, correlation length, and related properties) should be informed by process understanding or model-data mismatch statistics, which may favor shorter or more heterogeneous structures. However, under sparse observational coverage, such physically realistic choices may fail to sufficiently propagate observational information to the target fluxes. Conversely, stronger and smoother correlation structures may improve the mathematical efficiency of the inversion by allowing sparse observations to constrain wider regions, albeit at the cost of reduced physical specificity. The results presented here should therefore be interpreted not as prescribing a universally optimal prior structure, but rather as illustrating the practical consequences of this balance under current observational limitations. Although the resulting balance may be region-specific, the methodology used to identify an appropriate configuration is straightforward and can be readily adapted to regions beyond our study domain.

3.1.3 Multi-flux coexistence and signal "dilution"

The "resonance" effect, whereby coherent flux signals amplify correlations, implies a complementary phenomenon that can influence the spatial patterns of correlations: correlation "dilution" can occur when neighboring or coexisting flux types are uncorrelated. This is particularly relevant in atmospheric inversions, where multiple uncertain flux types jointly influence observed CO_2 concentrations. In F_{BIO} inversions, F_{ANT} is usually fixed to reduce the degree of freedom. This is a practical necessity because observations are limited and sparse. However, as mentioned earlier, this approach raises theoretical concerns since multiple flux types influence CO_2 concentrations and may exhibit correlation "dilution". Fixing one flux may alter the correlation between other fluxes and CO_2 concentrations, effectively removing the "dilution".

To assess the impact of fixing F_{ANT} on the correlations between F_{BIO} and CO_2 concentrations, as well as the implications of using the M_{ANT} tracer, we modeled three different CO_2 tracers corresponding to the three types of fluxes: M_{ANT}, M_{BIO}, and M_{OCE}. Figure 4 illustrates the correlations of tracers with their corresponding fluxes. Compared to the correlations obtained with all fluxes varying simultaneously (Fig. 1), fixing non-target fluxes leads to widespread and often substantial increases in correlation strength (e.g., compare Figs. 1a and 4a). These increases are most pronounced where M_{TOT} correlations were originally weak – for instance, especially for F_{ANT} in July, F_{BIO} in January, and F_{OCE} in both January and July. Conversely, the increases in correlations for F_{ANT} in January and F_{BIO} in July are less significant, as their correlations with for M_{TOT} are already strong at many sites.

The significant enhancement of correlations upon fixing other fluxes confirms that correlation "dilution" is a real effect in multiflux systems. A key implication is that simply fixing F_{ANT} in a F_{BIO} inversion may be methodologically problematic: the observational information that actually constrains F_{ANT} could be misattributed to F_{BIO}, distorting its solution. Conversely, at sites where M_{TOT} already shows strong correlations with a given flux (e.g., F_{ANT} in January or F_{BIO} in July), the correlation increases due to fixing other fluxes is minimal. This indicates that where information is intrinsically strong, random errors or uncertainties in coexisting fluxes have negligible "diluting" impact.

In summary, fixing F_{ANT} in the inversion of F_{BIO} can introduce disadvantages without offering significant benefits (except for numerical calculation). Nevertheless, these disadvantages will disappear if CO_2 tracer measurements are used instead of M_{TOT}. In such cases, when M_{TOT} are underestimated due to the underestimation of F_{ANT}, the M_{BIO} tracer remains unaffected, making the strong correlation beneficial. Currently, there is no simple M_{BIO} tracer, but the M_{ANT} tracer has been successfully applied in F_{ANT} inversions (Basu et al., 2016, 2020). However, some sites exhibit low correlations even for tracers (e.g., Fig. 4i), highlighting the limitations of using tracers. Conversely, as mentioned above, sites that show minimal correlation increases due to already strong correlations (e.g., Fig. 4b) may provide an opportunity to invert F_{ANT} effectively using M_{TOT} observations. It should be noted, however, this opportunity is not guaranteed but only works for some circumstances.

3.2 Temporal structures of concentration-flux correlations

3.2.1 Time variations of correlations

The temporal dynamics of the information transfer pathway are diagnosed by analyzing the time series of the Maximum Regional Correlation (MRC) within a $\sim 1200 \times 1200\,\text{km}^2$ domain surrounding each observation site. In Fig. 5, each line traces the evolution of the MRC between a flux impulse, of F_{ANT}, F_{OCE}, and F_{BIO} emitted at a specific hour, and the M_{TOT} at the site over subsequent hours. A key observation is the extensive overlap of these lines in many panels, indicating that the concentration at a given time exhibits similar correlation strength with flux impulses from many different prior hours. Conversely, where lines are separated, they reflect distinct correlation levels for fluxes emitted at different times for same source. Unlike the monotonic decay observed in space, these temporal MRC series frequently exhibit sustained plateaus or complex fluctuations patterns, changing with seasons and height. The MRCs for different flux types often vary in a complementary manner, as one weakens, another strengthens, particularly in regions of moderate correlation (e.g., Fig. 5c, f, and i). This anti-phase behavior suggests that shifting transport pathways alternately enhance the influence of different source regions at the receptor site.

The MRC evolution for ocean fluxes (F_{OCE}) shows distinct regimes across the observation network, reflecting the interplay of geography, atmospheric transport, and source-receptor connectivity. At predominantly remote oceanic or downwind coastal locations (e.g., Figs. 5o and S11 Ee), F_{OCE} exhibits dominant MRC. This occurs because these sites are persistently influenced by marine air masses, where the ocean source is strong and contiguous. However, its absolute MRC magnitude is moderated by the simultaneous presence and competition from co-varying terrestrial fluxes. A clear example is the Nansha site (e.g., Fig. S11Ee), where the column airmass is extremely minimally diluted by terrestrial fluxes, allowing a clear and stable oceanic signal to dominate the concentration variability; In contrast, at deep inland or strongly continentally influenced sites, the MRC for F_{OCE} is relatively low or even near zero. At first three stations in Fig. S11, where the marine air masses rarely reach the receptor under typical transport regimes, the MRC is zero. The majority stations, typically situated in coastal transition zones or eastern China (Fig. S11d, f, g, j, and k), show low, stable and dense MRC, displaying a characteristic of baseline ensemble. At these locations, the ocean-derived CO_2 contributes a persistent, near-constant background concentration.

The current features of site correlations related to ocean sources, which align intuitively with geography and climate, are largely attributable to and directly validate the reasonable prior's setting on perturbing monthly pCO_2 fields. Ocean surface pCO_2 and its fluxes vary slowly on synoptic scales, with dominant variations occurring on seasonal scales. Setting the prior temporal autocorrelation to 30 days essentially encodes this physical understanding into the inversion system. Consequently, the simulated information transfer pathways show that at sites influenced by the ocean, ocean signals manifest as a long-term, stable statistical entity. The reasonableness of site characteristics, such as which sites exhibit strong, moderate, or weak ocean influence, is precisely the

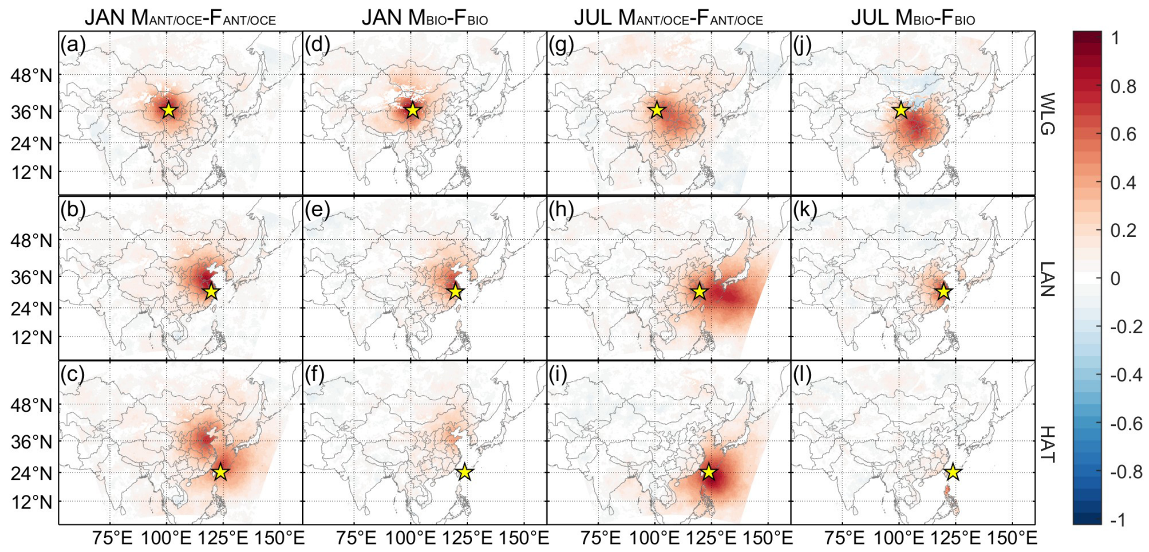

Figure 4. Spatial patterns of the tracer-flux correlations in different cases. Each row represents a site, labeled at right. **(a–c)** M_{ANT}-F_{ANT} and M_{OCE}-F_{OCE} in January; **(d–f)** M_{BIO}-F_{BIO} in January; **(g–l)** July.

expected outcome of this reasonable prior setting when processed through a realistic atmospheric transport model. If the ocean prior were set to a short decay time (e.g., 3 d), the system would assume that ocean flux information from a few days ago is nearly irrelevant, even at actual ocean sites. This would result in a loss of stable high correlations at ocean sites, replaced by rapidly decaying and highly fluctuating correlations and a disappearance of the "ocean background source" concept in the information transfer pathways, which would entirely contradict our fundamental physical understanding of ocean carbon exchange.

In contrast, the MRC for anthropogenic fluxes (F_{ANT}, grey lines) display highly heterogeneous and site-specific trajectories, including complex oscillations. This diversity should stem from the interaction between its prior specification and atmospheric dynamics, establishing a statistical tendency for information from older fluxes to weaken. In some extreme cases, the variation can show a decay trend rather than an oscillation (e.g., Figs. 5b and more prominently, Fig. S11Aw). However, at most of stations, this underlying decay of F_{ANT} is powerfully modulated by transport processes, such as shifting winds, boundary layer effect, creating complex fluctuations. A visible decay trend emerges only where transient transport variability is minimal (e.g., Fig. 5b), allowing the prior's statistical attenuation to be expressed clearly in the temporal trajectory of a single flux impulse's influence.

The biospheric fluxes (F_{BIO}, cyan lines) occasionally exhibit a separation into two parallel strata with distinct correlation levels, within which lines follow coherent, wave-like paths (Fig. 5p, see also Fig. S11). This pattern is a visual encoding of the prior's structural definition: daytime (GEE) and nighttime (RES) fluxes are treated as independent processes. The information pathway faithfully preserves this prescribed discontinuity, leading to the clustered strata. The coherent oscillations within each stratum reflect the diurnal and synoptic-scale variability of these biological signals as they are transported, illustrating how a process-informed prior structure is carried through the physical system. These non-monotonic behavior highlights the critical modulating role of atmospheric transport dynamics.

The similarities in MRC between CO_2 concentration and different fluxes at various hours enable the inversions of fluxes in a period using a single observation, thereby reducing the need for continuous monitoring at a site. This aligns with the discussion by Chevallier et al. (2012), which suggests that the temporal density of observations is much less informative than spatial coverage. However, high temporal density can be beneficial due to the variations in correlations between CO_2 concentration at various hours and a particular flux. If an observation with weak correlations to fluxes is used by chance, the inverted flux will not be optimal. High-density temporal observations can enhance the reliability of the information because a strong correlation at neighboring hours can complement a weak correlation at one hour. This is particularly important when strong correlations are rare and may be missed by low-density observations (e.g., Fig. S11Fi). Furthermore, obtaining a reliable estimation of fluxes from prior fluxes requires a sufficient combination of observations, as discussed in Sect. 3.1.1. Thus, high-density temporal observations can improve the robustness of flux inversions by reducing the influence of inaccuracies in concentration modeling that arise from factors other than uncertain fluxes, ultimately leading to more accurate and reliable results.

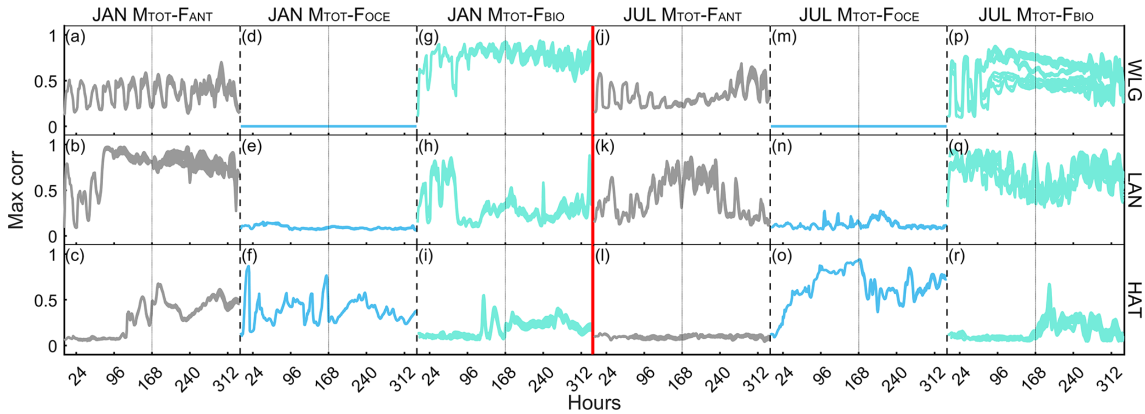

Figure 5. Timeseries of maximum correlations the 168th-h M_{TOT} at sites and the 0th-h fluxes (F_{ANT}, F_{OCE}, and F_{BIO}) near the sites. Each row represents a site, labeled at right. **(a–c)** M_{TOT}-F_{ANT} in January; **(d–f)** M_{TOT}-F_{OCE} in January; **(g–i)** M_{TOT}-F_{BIO} in January, **(j–r)** July.

3.2.2 Multi-flux coexistence revisited

It is observed in Sect. 3.2.1 that the MRC at an observation site for different flux types often vary in a complementary manner. This can be more clearly illustrated when we spread the "observation sites" on the whole domain: we calculate the MRC for an observation site in Fig. 5, and this calculation is then applied across all model grids to generate Fig. 6 for specific times.

Like the temporally complementary variation of different fluxes in Fig. 5, the three types of fluxes exhibit spatially complementary distributions in Fig. 6. In January, most areas in China, South Korea, and Japan show relatively strong correlations between surface CO_2 and F_{ANT}, with numerous small hotspots in India and Central Asia (Fig. 5a–c). Other land areas generally show strong correlations between surface CO_2 and F_{BIO} (Fig. 5g–i). In the continental seas near China, South Korea, and Japan, the correlations between surface CO_2 and F_{ANT} are also strong. In contrast, the southern continental seas display stronger correlations between surface CO_2 and F_{BIO}. In contrast, the open ocean, distant from the continent, shows strong correlations between surface CO_2 and F_{OCE} (Fig. 5m–o). In July, the overall patterns are similar, but the influence of F_{ANT} becomes concentrated in smaller areas (Fig. 5d–f). Meanwhile, the influence of F_{BIO} increases significantly in southern China, Korea, and Japan (Fig. 5d–f); however, the two-week-average does not increase very significantly due to the larger diurnal variations of correlations in July (compare Fig. 5a and c, F_{BIO}). Over the ocean, the influence of F_{OCE} becomes much stronger than in January, especially in the Indian Ocean and along the western margin of the Pacific Ocean (Fig. 5p–r).

The complementary distributions of MRCs for different types of fluxes implies the signal "dilution" discussed in Sect. 3.1.3 from another point of view. When some type of flux (e.g., F_{ANT}) is fixed, the MRC of that type of flux will be zero, and therefore the other type of flux will fill the absent MRC. Consequently, there will be signal misattributions.

There is another implication of Fig. 6. A large value means a strong correlation between surface CO_2 and nearby fluxes, suggesting that observations from these locations can be effectively used to invert fluxes. In other words, observation data collected from areas with strong correlations provide more valuable information about fluxes, making these locations ideal for establishing measurement sites. Conversely, sites located in areas with weak correlation are less informative for flux inversion. Since atmospheric transport plays a critical role in determining the locations of high correlations, and because atmospheric dynamics can vary rapidly and substantially (see also the January–July contrast in Fig. 6), the optimal measurement locations may change quickly; therefore, our findings should not be regarded as definitive. However, the complementary distributions of correlations for different fluxes highlight the potential for identifying new measurement sites based on the correlation analysis.

3.3 Comparison with 4D-Var

Many inversion systems are based on 4D-Var. These systems also encounter a similar information transfer problem: how observations influence the unobserved fluxes. Here, we analyze this problem for a 4D-Var system. However, this analysis is partial because the solution to the inverse problem is iterative.

The starting point of 4D-Var is a cost function $J(\boldsymbol{E}) = 1/2\left(\boldsymbol{E}-\boldsymbol{E}^{\mathrm{b}}\right)^T \mathbf{B}^{-1}\left(\boldsymbol{E}-\boldsymbol{E}^{\mathrm{b}}\right)+1/2\left(\boldsymbol{y}^{\mathrm{b}}-\boldsymbol{y}^{\mathrm{o}}\right)^T \mathbf{R}^{-1}(\boldsymbol{y}^{\mathrm{b}}-\boldsymbol{y}^{\mathrm{o}})$, and the goal is to minimize the cost function iteratively based on the gradient $\mathbf{g} := \partial J/\partial \boldsymbol{E}$. The iteration directions, which are closely related to the gradients, determine how the fluxes are modified after assimilating observations and can thus be interpreted as information transfer pathways. Since fluxes are typically modified most significantly in the first few iterations (see Fig. 4 of Niwa et al., 2022), the overall iteration direction may be roughly approximated by the first iteration direction.

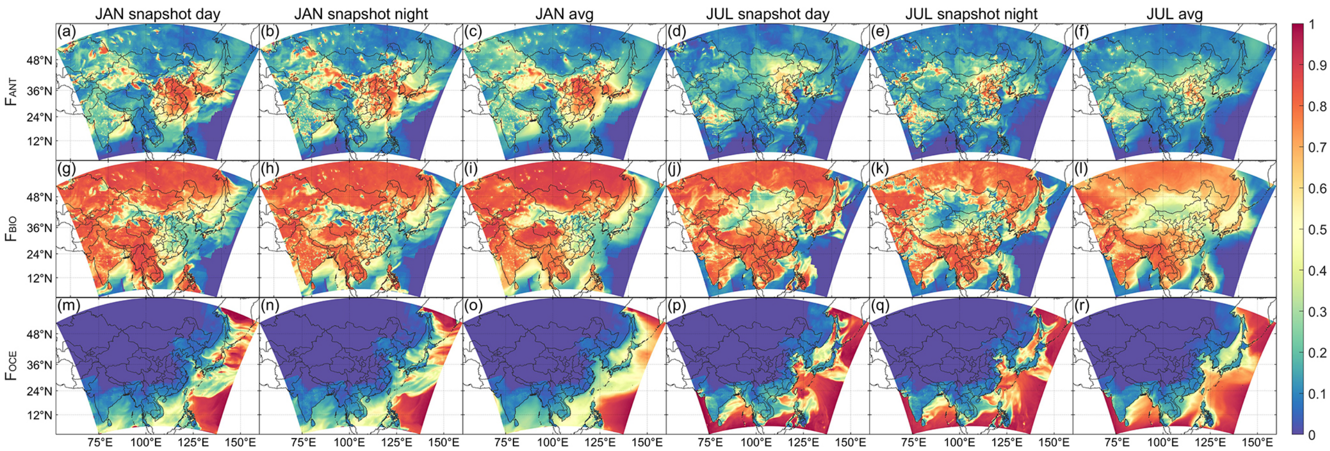

Figure 6. Maximum absolute values of correlation coefficients between surface M_{TOT} at a model grid and nearby (a $\sim 1200 \times 1200\,\mathrm{km}^2$ box) fluxes. **(a)** the 168th-h M_{TOT} and the 0th-h F_{ANT} in January; **(b)** the 180th-h M_{TOT} and the 12th-h F_{ANT} **(c)** two weeks average of M_{TOT}-F_{ANT} at 00:00, 06:00, 12:00, and 18:00 on each day; **(d–f)** July; **(g–l)** F_{BIO}; **(m–r)** F_{OCE}.

The gradient has two parts, which can be better understood by defining $J_{\boldsymbol{y}} := 1/2\left(\boldsymbol{y}^{\mathrm{b}} - \boldsymbol{y}^{\mathrm{o}}\right)^T \mathbf{R}^{-1}\left(\boldsymbol{y}^{\mathrm{b}} - \boldsymbol{y}^{\mathrm{o}}\right)$. Thus, the gradient is given by $\mathbf{g} = \mathbf{B}^{-1}\left(\boldsymbol{E} - \boldsymbol{E}^{\mathrm{b}}\right) + \partial J_{\boldsymbol{y}}/\partial \boldsymbol{E}$. The first part $\mathbf{B}^{-1}\left(\boldsymbol{E} - \boldsymbol{E}^{\mathrm{b}}\right)$ can be directly calculated if $\mathbf{B}$ is invertible, while the second part usually relies on adjoint models of transport models. Here we use the CMAQ (v5.0) model and its adjoint, CMAQ-ADJ (Zhao et al., 2020), to calculate this part of the gradient. Choosing the 24 surface sites to form the cost function, with pseudo-observations $\boldsymbol{y}^{\mathrm{o}}$ from the independent run (see Sect. 2.3) and setting the observation variances to 2.5 ppmv^2 for simplicity, we obtain $\partial J_{\boldsymbol{y}}/\partial \boldsymbol{E}$ (Fig. 7A) which is the gradient $\mathbf{g}_0$ since $\boldsymbol{E} = \boldsymbol{E}^{\mathrm{b}}$. It can be seen that the gradients with respect to daily fluxes are concentrated on a very small neighborhood of observation sites, resembling concentration footprints (see Fig. 4 of Storm et al., 2023).

Next, we calculate the iteration direction. Suppose we use the simple steepest descent method in the iteration. In that case, the iteration direction at the first iteration will be $-\mathbf{g}_0$, meaning only fluxes in areas very close to observation sites are modified after assimilating observations. At the second iteration, we obtain the new gradient $\mathbf{g}_1 = \mathbf{B}^{-1}\left(\boldsymbol{E} - \boldsymbol{E}^{\mathrm{b}}\right) + \frac{\partial J_{\boldsymbol{y}}}{\partial \boldsymbol{E}} = -\gamma \mathbf{B}^{-1}\mathbf{g}_0 + \partial J_{\boldsymbol{y}}/\partial \boldsymbol{E}$, where γ is the step size of the first iteration. Even if $\mathbf{B}$ is invertible and computationally feasible to calculate, $\mathbf{B}^{-1}\mathbf{g}_0$ will still be concentrated in a small neighborhood around the observation sites. As a result, fluxes cannot be significantly modified after assimilating observations except for areas close to observation sites.

In practice, other methods than the simple steepest descent method are used, such as conjugate gradient and quasi-Newton methods (Chevallier et al., 2007; Niwa et al., 2017b), and specific techniques can expand the regions where fluxes can be modified (Fisher, 1998). In both methods, the key is to calculate $\mathbf{Bg}$ (possibly with some modifications) instead of $\mathbf{B}^{-1}\mathbf{g}$. From the perspective of Newton's methods, this is equivalent to approximating the Hessian, $\mathbf{B}^{-1} + \mathbf{H}^T\mathbf{R}^{-1}\mathbf{H}$, with $\mathbf{B}^{-1}$, and the iterations may be seen as refinements of this approximation. Using the same correlation function as in the OFF600 case and a uniform standard deviation of $10\,\mathrm{mol\,s^{-1}\,grid^{-1}}$ ($\sim 0.0142\,\mathrm{gC\,m^{-2}\,d^{-1}}$), we calculate $\mathbf{Bg}_0$ (Fig. 7B). The areas where fluxes can be modified are significantly enlarged compared to $\mathbf{g}_0$ (Fig. 7A) but remain concentrated around observation sites. Additionally, these areas are similar to the patterns of correlation functions and concentration-flux correlation patterns in Monte Carlo simulations (e.g., Fig. 4) after possible weightings. Therefore, similar to KF-based systems, 4D-Var-based inversion systems also rely heavily on background correlation functions to transfer observational information (via the regularization term $1/2\left(\boldsymbol{E} - \boldsymbol{E}^{\mathrm{b}}\right)^T \mathbf{B}^{-1}\left(\boldsymbol{E} - \boldsymbol{E}^{\mathrm{b}}\right)$), while transport plays only a minor role in determining the spatial and temporal extent of the inversion (though not the strength). This minor contribution arises because the cost function gradient is restricted to small areas around observation sites. Indeed, if we retain only the gradient values very near observation sites while setting "remote" gradients to zero, the patterns of $\mathbf{Bg}_0$ remain unchanged to a large extent (Fig. S12). This minor contribution does not change even when extending the simulation time, as demonstrated by the one-month results (Fig. 7C and D).

In summary, consistent with previous studies demonstrating the equivalence between the Kalman filter update and the 4D-Var cost-function solution – both in theoretical analyses (Evensen et al., 2022) and in comparisons of posterior estimates from the two approaches (Liu et al., 2016) – our analysis provides an intuitive illustration of this corresponding equivalence under linear–Gaussian assumptions. However, since KF is typically implemented as EnKF, the small ensemble size can lead to spurious correlations (Fig. S6), necessitating localization in EnKF. This means the spatial extents of the two solutions may differ, especially in observation-sparse areas (Liu et al., 2016).

With these insights into the 4D-Var method, we can better understand why the spatial patterns of concentration-flux correlations are primarily shaped by flux autocorrelations, as previously discussed for EnKF. Since the first-order sensitivity of concentrations to fluxes is limited to small areas, concentration-flux correlations are likely constrained to small areas. However, flux-flux autocorrelations are strong over larger regions (depending on the correlation functions), meaning that concentration-flux correlations can extend over larger areas due to the transitivity of strong correlations (Sotos et al., 2009). In this way, the prior information embedded in the background covariance matrix plays a role in transferring information from observed concentrations to unobserved fluxes.

Finally, it should be noted that the above discussion assumes continuous observation data. Under these conditions, the cost function gradient is continuously "renewed" as new observation data enter, ensuring that large gradient values persist near observation sites. If observation data are instantaneous, the gradient will not show large values for fluxes remote in time, making it appear extended in space (see Fig. S13). This is the typical way results related to gradients or sensitivities are presented in previous studies (e.g., Liu et al., 2015; Niwa et al., 2017a). However, since the largest gradient values always appear near (both in time and space) the observations, and these values are the most critical for assimilation, analysis based on instantaneous observations may not directly apply to understanding inversion systems. If only a single observation time is used to invert yearly or monthly fluxes, incidental transport errors at that time may significantly distort results, as no other observations are available to compensate for such errors. However, in observation-sparse areas, remote observations may still provide valuable information, which could also contribute to the differences between EnKF and 4D-Var, as EnKF cannot utilize remote observations effectively.

4 Limitations and future work

This study excludes the impact of transport errors when analyzing the EnKF solution for flux inversions due to the complexity of the inversion system. Munassar et al. (2023) demonstrated that variations in transport models can lead to discrepancies exceeding 50 % between two inversion systems. Consequently, it is essential to investigate how these transport errors affect the inversion results and, more precisely and more relevant to this study, how they may influence the correlation patterns of unobserved fluxes and observed concentrations. Such an analysis could serve as a natural extension of the work by Chen et al. (2019), which primarily examined variances. Transport errors will likely influence correlations and variances, potentially leading to less distinct correlation patterns than those presented in this study.

This study also overlooks the variability of boundary conditions of CO_2 concentrations, which is the second most important factor contributing to the discrepancies in different regional inversion systems, as shown by Munassar et al. (2023). While we might expect the influence of BCs on correlation patterns to be minimal, similar to the small impacts of initial conditions, this assumption may warrant further investigation. This will be investigated in a following study.

Our analysis does not include the chemical production of CO_2 from the oxidation of CH_4 and CO, which can be a non-negligible source in regions with intensive fossil fuel extraction (e.g., coal-mining areas) and may influence modeled concentration-flux correlations (e.g., Wang et al., 2025). Additionally, the model's representation of vertical transport and mixing over complex terrain (such as the Tibetan Plateau and the Shanxi-Shaanxi region) is subject to uncertainties that could affect correlation patterns at high-altitude sites (e.g., Wang et al., 2022). The temporal distribution of anthropogenic emissions may smooth holidays and business-cycles, and does not fully capture day-to-day emissions changes from fires or monsoons. Finally, nonlinear spatial propagation of observational uncertainty may not be fully captured by the modeling system (e.g., Kurosawa and Poterjoy, 2021). These limitations should be considered when interpreting the spatial patterns shown in our diagnostic maps, though they are not expected to alter the conclusions regarding the role of prior correlation length scales.

It is important to clarify that a small influence on correlation patterns does not necessarily mean a small influence on inversion results. While correlation is a key parameter that characterizes the transfer of information from observed concentrations to unobserved fluxes, it does not determine the overall "content" of information. Efficient information transfer does not imply that the information itself is abundant. More technically, inversion results depend not only on the covariance matrix but also on the innovations, which are determined by the differences between modeled concentrations and observations. These innovations can be affected by transport errors, uncertainties in initial and boundary conditions, and other factors. Consequently, these factors can significantly influence inversion results. This study does not address uncertainties in modeling concentrations and, therefore, presents only a partial view of the overall situation.

In the analysis of the 4D-Var, only the first iteration is examined. This may be valid when the approximation of the Hessian $\mathbf{B}^{-1}+\mathbf{H}^T\mathbf{R}^{-1}\mathbf{H}$ by $\mathbf{B}^{-1}$ is reasonable. In a complete 4D-Var system, iterations are further complicated by the variances of the prior fluxes, and an analysis based on normalization that removes the influence of variances becomes more challenging. Nevertheless, examining results from additional iterations would be beneficial, even through an analysis based on iteration-by-iteration normalizations.

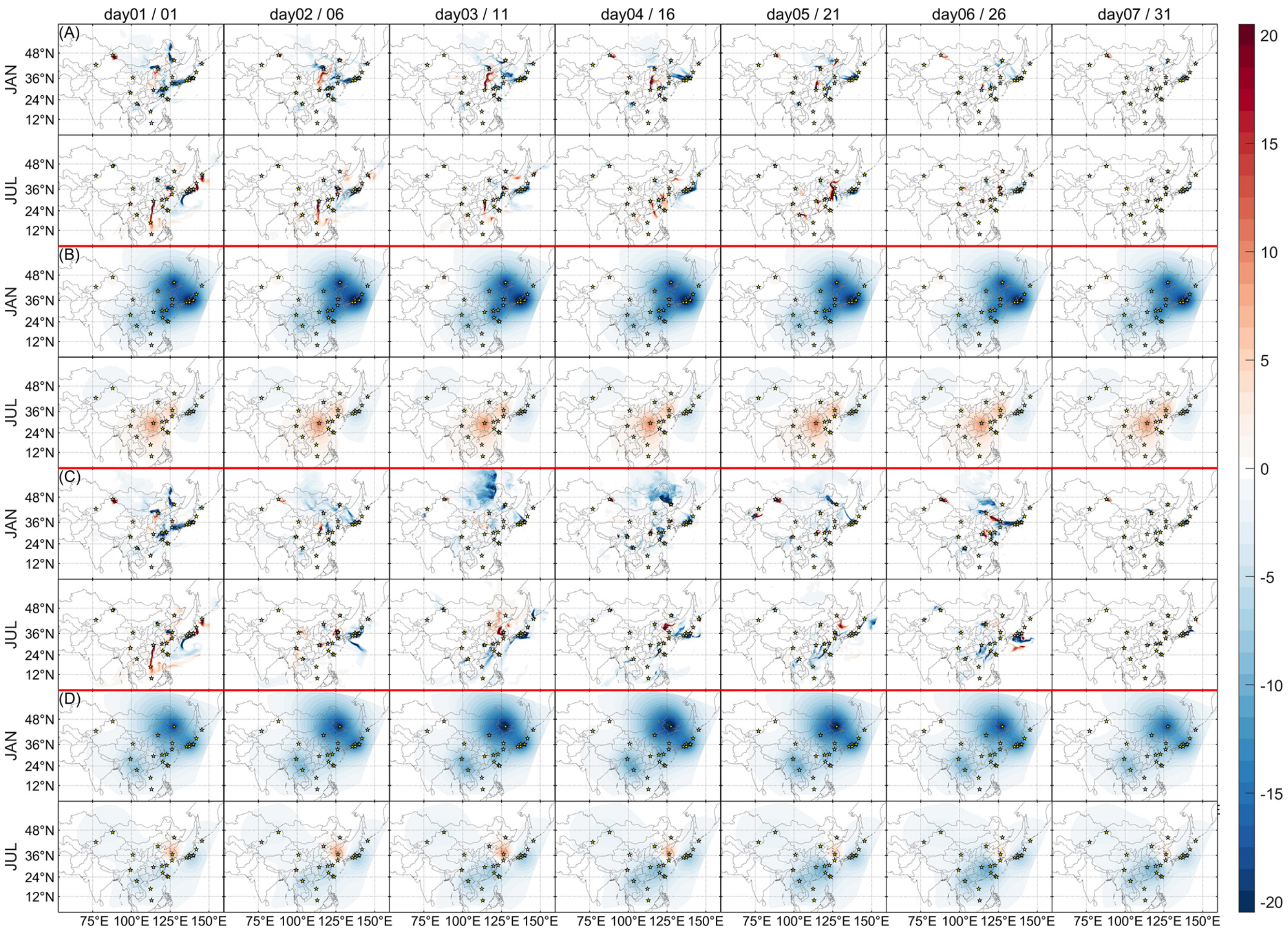

Figure 7. Spatial patterns of daily gradients and iteration directions. **(A)** is the gradient of the cost function to the daily fluxes. **(B)** is the iteration directions of the first iteration, $\mathbf{Bg}_0$, and is calculated using the same correlation function as in case OFF600 and a uniform standard deviation of $10\,\mathrm{mol\,s^{-1}\,grid^{-1}}$ ($\sim 0.0142\,\mathrm{gC\,m^{-2}\,d^{-1}}$). Rows represent different months, and columns represent different days. **(C)** and **(D)** are the same as **(A)** and **(B)** but for the 1-month simulation. The values of **(D)** are divided by four (four weeks) for the purpose of illustration. The unit of **(A)** and **(C)** is $(\mathrm{gC\,m^{-2}\,d^{-1}})^{-1}$, and of **(B)** and **(D)** is $\mathrm{gC\,m^{-2}\,d^{-1}}$.

Finally, this study serves as an initial analysis of how observed CO_2 concentrations are utilized to invert unobserved fluxes, focusing specifically on correlations at particular locations and times. As previously mentioned, inversion results represent a combination of various monotonic changes relative to prior fluxes. However, it remains unclear how this combination yields reliable inversion outcomes.

5 Conclusions

There is an urgent need for reliable CO_2 flux inversions to address the challenges of climate change. This study adopts a diagnostic perspective aimed at elucidating the internal information transfer mechanisms of inversion systems, analyzing the core process by which observational information is translated into flux estimates in atmospheric CO_2 inversions. Through a combination of large-ensemble (EnKF) Monte Carlo simulations and comparative analysis with the 4D-Var method, we have clearly articulated and quantified the decisive role of the prior flux covariance structure in shaping and dominating the entire information flow.

Our findings show that spatiotemporal scales of information transfer are primarily set by the autocorrelation structure of the prior fluxes, while atmospheric transport processes primarily modulate the specific morphology of correlations at individual sites (e.g., directionality and asymmetry). Flux autocorrelations induce “resonance” and “dilution” effects that profoundly impact inversion efficiency and accuracy. When fluxes are strongly positively correlated over a large region (long autocorrelation length), their released CO_2 signals coherently superimpose during transport, producing a “resonance” effect that enhances the maximum concentration-flux correlation. Conversely, when multiple flux types (e.g., anthropogenic and biospheric) coexist and are uncorrelated, their signals interfere with each other, causing a "dilution" effect that weakens the discernible correlation between any single flux type and the total concentration. This explains why, under sparse observations, using overly short autocorrelation lengths (e.g., < 100 km) not only shrinks the spatial influence of information but also systematically reduces the information extraction efficiency of the inversion system, leading to extensive "blank areas" of observational constraint (Fig. 3). It should be emphasized, however, that the choice of longer autocorrelation lengths (e.g., the 600 km recommendation for the current East Asian network) involves a trade-off between physical realism and mathematical efficiency. This choice is conditional on network sparsity and is region-specific. As observation networks become denser in the future, the optimal correlation length will converge toward the shorter, physically realistic scale. Our methodological framework provides a quantitative tool to reevaluate this optimal length as observational constraints improve.

A direct consequence of the "dilution" effect is that when inverting one flux type (e.g., F_{BIO}), simply fixing another (e.g., F_{ANT}) misattributes observational information originally meant to constrain the fixed flux to the target flux, thereby distorting its solution. This misallocation is particularly severe in regions where the target flux itself has a weak correlation with the total concentration. Using flux-specific tracers (e.g., $^{14}CO_2$) is the fundamental way to avoid this issue. However, in the absence of tracers, the interactions among multiple fluxes must be fully recognized and handled with caution.

Comparative analysis with the 4D-Var framework reveals that its information transfer also relies heavily on the prior covariance $\mathbf{B}$. The adjoint-derived gradient is inherently local; it is the scaling by the $\mathbf{B}$ matrix that projects observational influence to broader areas. Consistent with the theoretical equivalence between the Kalman filter update and the 4D-Var cost-function solution under linear–Gaussian assumptions (Evensen et al., 2022), as well as previous inversion studies showing similar posterior estimates from the two approaches in observation-constrained regions (Liu et al., 2016), our analysis suggests a corresponding equivalence in their information-transfer kernel under these assumptions. Both utilize the prior covariance matrix as the conduit to distribute the constraint from point observations across larger space and time. Their primary practical differences stem from the spurious correlations in EnKF due to limited ensemble size and the consequent need for localization.

This study elucidates the fundamental principles governing the transfer of observational information in CO_2 flux inversions by establishing a mechanism-diagnostic ensemble simulation framework. Moving beyond the traditional evaluation of final flux estimates, we dissect the internal workings of data assimilation systems, revealing the decisive role of the prior error covariance structure in shaping the information propagation pathways. By making the internal process of constraint propagation explicit, we lay the foundation for building more transparent, interpretable, and trustworthy flux estimation systems.

Data availability. The metadata for the surface CO_2 observation data can be obtained from the World Data Centre for Greenhouse Gases (WDCGG) at https://gaw.kishou.go.jp/ (World Data Centre for Greenhouse Gases, 2025). The satellite XCO_2 data can be accessed through the Goddard Earth Sciences Data and Information Services Center (GES DISC) at https://doi.org/10.5067/5Q8JLZL1VD4A (OCO-2/OCO-3 Science Team et al., 2024).

Supplement. The supplement related to this article is available online at https://doi.org/10.5194/acp-26-9257-2026-supplement.

Author contributions. YL designed the study and edited the manuscript. SF ran the simulations, conducted analyses, and wrote the manuscript.

Competing interests. The contact author has declared that none of the authors has any competing interests.

Disclaimer. Publisher's note: Copernicus Publications remains neutral with regard to jurisdictional claims made in the text, published maps, institutional affiliations, or any other geographical representation in this paper. The authors bear the ultimate responsibility for providing appropriate place names. Views expressed in the text are those of the authors and do not necessarily reflect the views of the publisher.

Acknowledgements. We thank Shenzhen Key Laboratory of Marine Archaea Geo-Omics, Southern University of Science and Technology (SUSTech). This paper also contributes to the Science Plan of the UN Ocean Decade Global Ocean Negative Carbon Emissions (Global ONCE) Program and its first project iCUBEs (#52.2). We thank the Center for Computational Science and Engineering at Southern University of Science and Technology.

Financial support. This research has been supported by the National Natural Science Foundation of China (grant nos. 42471393, 41961160728, 41575106, 42105124, and 41905114), the Shenzhen Science and Technology Innovation Program (grant nos. KCXFZ20230731094301004, KCXFZ20211020174803OO, and KQTD20180411143441009).

Review statement. This paper was edited by Jason Cohen and reviewed by two anonymous referees.

References

Ahmadov, R., Gerbig, C., Kretschmer, R., Koerner, S., Neininger, B., Dolman, A. J., and Sarrat, C.: Mesoscale covariance of transport and CO_2 fluxes: Evidence from observations and simulations using the WRF-VPRM coupled atmosphere-biosphere model, J. Geophys. Res.-Atmos., 112, https://doi.org/10.1029/2007jd008552, 2007.

Asch, M., Bocquet, M., and Nodet, M.: Data Assimilation: Methods, Algorithms, and Applications, Society for Industrial and Applied Mathematics, https://doi.org/10.1137/1.9781611974546, 2016.

Basu, S., Miller, J. B., and Lehman, S.: Separation of biospheric and fossil fuel fluxes of CO_2 by atmospheric inversion of CO_2 and $^{14}CO_2$ measurements: Observation System Simulations, Atmos. Chem. Phys., 16, 5665–5683, https://doi.org/10.5194/acp-16-5665-2016, 2016.

Basu, S., Lehman, S. J., Miller, J. B., Andrews, A. E., Sweeney, C., Gurney, K. R., Xu, X., Southon, J., and Tans, P. P.: Estimating US fossil fuel CO_2 emissions from measurements of C-14 in atmospheric CO_2, P. Natl. Acad. Sci. USA, 117, 13300–13307, https://doi.org/10.1073/pnas.1919032117, 2020.

Beck, V., Koch, T., Kretschmer, R., Marshall, J., Ahmadov, R., Gerbig, C., Pillai, D., and Heimann, M.: The WRF Greenhouse Gas Model (WRF-GHG), Max-Planck-Institut für Biogeochemie, https://www.bgc-jena.mpg.de/5363366/tech_report25.pdf (last access: 23 June 2026), 2011.

Chandra, N., Patra, P. K., Niwa, Y., Ito, A., Iida, Y., Goto, D., Morimoto, S., Kondo, M., Takigawa, M., Hajima, T., and Watanabe, M.: Estimated regional CO_2 flux and uncertainty based on an ensemble of atmospheric CO_2 inversions, Atmos. Chem. Phys., 22, 9215–9243, https://doi.org/10.5194/acp-22-9215-2022, 2022.

Chen, H. W., Zhang, F., Lauvaux, T., Davis, K. J., Feng, S., Butler, M. P., and Alley, R. B.: Characterization of Regional-Scale CO_2 Transport Uncertainties in an Ensemble with Flow-Dependent Transport Errors, Geophys. Res. Lett., 46, 4049–4058, https://doi.org/10.1029/2018GL081341, 2019.

Chen, H. W. W., Zhang, F., Lauvaux, T., Scholze, M., Davis, K. J. J., and Alley, R. B. B.: Regional CO_2 Inversion Through Ensemble-Based Simultaneous State and Parameter Estimation: TRACE Framework and Controlled Experiments, J. Adv. Model. Earth Syst., 15, https://doi.org/10.1029/2022ms003208, 2023.

Chevallier, F.: Fluxes of Carbon Dioxide From Managed Ecosystems Estimated by National Inventories Compared to Atmospheric Inverse Modeling, Geophys. Res. Lett., 48, https://doi.org/10.1029/2021gl093565, 2021.

Chevallier, F., Fisher, M., Peylin, P., Serrar, S., Bousquet, P., Breon, F. M., Chedin, A., and Ciais, P.: Inferring CO_2 sources and sinks from satellite observations: Method and application to TOVS data, J. Geophys. Res.-Atmos., 110, https://doi.org/10.1029/2005jd006390, 2005.

Chevallier, F., Breon, F.-M., and Rayner, P. J.: Contribution of the Orbiting Carbon Observatory to the estimation of CO_2 sources and sinks: Theoretical study in a variational data assimilation framework, J. Geophys. Res.-Atmos., 112, https://doi.org/10.1029/2006jd007375, 2007.

Chevallier, F., Wang, T., Ciais, P., Maignan, F., Bocquet, M., Arain, M. A., Cescatti, A., Chen, J., Dolman, A. J., Law, B. E., Margolis, H. A., Montagnani, L., and Moors, E. J.: What eddy-covariance measurements tell us about prior land flux errors in CO_2-flux inversion schemes, Global Biogeochem. Cy., 26, https://doi.org/10.1029/2010gb003974, 2012.

Crippa, M., Solazzo, E., Huang, G., Guizzardi, D., Koffi, E., Muntean, M., Schieberle, C., Friedrich, R., and Janssens-Maenhout, G.: High resolution temporal profiles in the Emissions Database for Global Atmospheric Research, Sci. Data, 7, https://doi.org/10.1038/s41597-020-0462-2, 2020.

Dong, X., Yue, M., Jiang, Y., Hu, X.-M., Ma, Q., Pu, J., and Zhou, G.: Analysis of CO_2 spatio-temporal variations in China using a weather–biosphere online coupled model, Atmos. Chem. Phys., 21, 7217–7233, https://doi.org/10.5194/acp-21-7217-2021, 2021.

Evensen, G., Vossepoel, F. C., and Van Leeuwen, P. J.: Data Assimilation Fundamentals: A Unified Formulation of the State and Parameter Estimation Problem, Springer International Publishing, Cham, https://doi.org/10.1007/978-3-030-96709-3, 2022.

Fan, S. and Li, Y.: The impacts of marine-emitted halogens on OH radicals in East Asia during summer, Atmos. Chem. Phys., 22, 7331–7351, https://doi.org/10.5194/acp-22-7331-2022, 2022.

Fan, S. and Li, Y.: Potential deterioration of ozone pollution in coastal areas caused by marine-emitted halogens: A case study in the Guangdong-Hong Kong-Macao Greater Bay Area, Sci. Total Environ., 860, 160456, https://doi.org/10.1016/j.scitotenv.2022.160456, 2023.

Fan, S., Li, Y., and Liu, C.: Are Environmentally Friendly Fireworks Really "Green" for Air Quality? A Study from the 2019 National Day Fireworks Display in Shenzhen, Environ. Sci. Technol., 55, 3520–3529, https://doi.org/10.1021/acs.est.0c03521, 2021.

Fay, A. R., Gregor, L., Landschützer, P., McKinley, G. A., Gruber, N., Gehlen, M., Iida, Y., Laruelle, G. G., Rödenbeck, C., Roobaert, A., and Zeng, J.: SeaFlux: harmonization of air–sea CO_2 fluxes from surface pCO_2 data products using a standardized approach, Earth Syst. Sci. Data, 13, 4693–4710, https://doi.org/10.5194/essd-13-4693-2021, 2021.

Fisher, M.: Minimization algorithms for variational data assimilation, in: Seminar on Recent Developments in Numerical Methods for Atmospheric Modelling, 7–11 September 1998, https://www.ecmwf.int/en/elibrary/74480-minimization-algorithms-variational-data-assimilation (last access: 23 June 2026), 1998.

Friedlingstein, P., O'Sullivan, M., Jones, M. W., Andrew, R. M., Hauck, J., Landschützer, P., Le Quéré, C., Li, H., Luijkx, I. T., Olsen, A., Peters, G. P., Peters, W., Pongratz, J., Schwingshackl, C., Sitch, S., Canadell, J. G., Ciais, P., Jackson, R. B., Alin, S. R., Arneth, A., Arora, V., Bates, N. R., Becker, M., Bellouin, N., Berghoff, C. F., Bittig, H. C., Bopp, L., Cadule, P., Campbell, K., Chamberlain, M. A., Chandra, N., Chevallier, F., Chini, L. P., Colligan, T., Decayeux, J., Djeutchouang, L. M., Dou, X., Duran Rojas, C., Enyo, K., Evans, W., Fay, A. R., Feely, R. A., Ford, D. J., Foster, A., Gasser, T., Gehlen, M., Gkritzalis, T., Grassi, G., Gregor, L., Gruber, N., Gürses, Ö., Harris, I., Hefner, M., Heinke, J., Hurtt, G. C., Iida, Y., Ilyina, T., Jacobson, A. R., Jain, A. K., Jarníková, T., Jersild, A., Jiang, F., Jin, Z., Kato, E., Keeling, R. F., Klein Goldewijk, K., Knauer, J., Korsbakken, J. I., Lan, X., Lauvset, S. K., Lefèvre, N., Liu, Z., Liu, J., Ma, L., Maksyutov, S., Marland, G., Mayot, N., McGuire, P. C., Metzl, N., Monacci, N. M., Morgan, E. J., Nakaoka, S.-I., Neill, C., Niwa, Y., Nützel, T., Olivier, L., Ono, T., Palmer, P. I., Pierrot, D., Qin, Z., Resplandy, L., Roobaert, A., Rosan, T. M., Rödenbeck, C., Schwinger, J., Smallman, T. L., Smith, S. M., Sospedra-Alfonso, R., Steinhoff, T., Sun, Q., Sutton, A. J., Séférian, R., Takao, S., Tatebe, H., Tian, H., Tilbrook, B., Torres, O., Tourigny, E., Tsujino, H., Tubiello, F., van der Werf, G., Wanninkhof, R., Wang, X., Yang, D., Yang, X., Yu, Z., Yuan, W., Yue, X., Zaehle, S., Zeng, N., and Zeng, J.: Global Carbon Budget 2024, Earth Syst. Sci. Data, 17, 965–1039, https://doi.org/10.5194/essd-17-965-2025, 2025.

Gao, J., Li, Y., Xie, Z., Hu, B., Wang, L., Bao, F., and Fan, S.: The impact of the aerosol reduction on the worsening ozone pollution over the Beijing-Tianjin-Hebei region via influencing photolysis rates, Sci. Total Environ., 821, https://doi.org/10.1016/j.scitotenv.2022.153197, 2022.

Gaspari, G. and Cohn, S. E.: Construction of correlation functions in two and three dimensions, Q. J. Roy. Meteorol. Soc., 125, 723–757, https://doi.org/10.1002/qj.49712555417, 1999.

Global Atmosphere Watch Station Information System: Locations of Observation Sites, https://gawsis.meteoswiss.ch/GAWSIS/#/, last access: 28 April 2024.

Gourdji, S. M., Karion, A., Lopez-Coto, I., Ghosh, S., Mueller, K. L., Zhou, Y., Williams, C. A., Baker, I. T., Haynes, K. D., and Whetstone, J. R.: A Modified Vegetation Photosynthesis and Respiration Model (VPRM) for the Eastern USA and Canada, Evaluated With Comparison to Atmospheric Observations and Other Biospheric Models, J. Geophys. Res.-Biogeosci., 127, https://doi.org/10.1029/2021jg006290, 2022.

Houtekamer, P. L. and Mitchell, H. L.: A Sequential Ensemble Kalman Filter for Atmospheric Data Assimilation, Mon. Weather Rev., 129, 123–137, https://doi.org/10.1175/1520-0493(2001)129<0123:ASEKFF>2.0.CO;2, 2001.

IPCC AR6: Climate Change 2021: The Physical Science Basis. Contribution of Working Group I to the Sixth Assessment Report of the Intergovernmental Panel on Climate Change, https://doi.org/10.1017/9781009157896, 2021.

Jacobson, A. R., Schuldt, K. N., Tans, P., Andrews, A., Miller, J. B., Oda, T., Basu, S., Mund, J., Weir, B., Ott, L., Aalto, T., Abshire, J. B., Aikin, K., Aoki, S., Apadula, F., Arnold, S., Baier, B., Bartyzel, J., Beyersdorf, A., Biermann, T., Biraud, S. C., Boenisch, H., Brailsford, G., Brand, W. A., Chen, G., Chen, H., Chmura, L., Clark, S., Colomb, A., Commane, R., Conil, S., Couret, C., Cox, A., Cristofanelli, P., Cuevas, E., Curcoll, R., Daube, B., Davis, K. J., De Wekker, S., Della Coletta, J., and et al.: CarbonTracker CT2022, https://doi.org/10.25925/z1gj-3254, 2023.

Janssens-Maenhout, G., Crippa, M., Guizzardi, D., Muntean, M., Schaaf, E., Dentener, F., Bergamaschi, P., Pagliari, V., Olivier, J. G. J., Peters, J. A. H. W., van Aardenne, J. A., Monni, S., Doering, U., Petrescu, A. M. R., Solazzo, E., and Oreggioni, G. D.: EDGAR v4.3.2 Global Atlas of the three major greenhouse gas emissions for the period 1970–2012, Earth Syst. Sci. Data, 11, 959–1002, https://doi.org/10.5194/essd-11-959-2019, 2019.

Jin, Z., Wang, T., Zhang, H., Wang, Y., Ding, J., and Tian, X.: Constraint of satellite CO_2 retrieval on the global carbon cycle from a Chinese atmospheric inversion system, Sci. China-Earth Sci., 66, 609–618, https://doi.org/10.1007/s11430-022-1036-7, 2023.

Kountouris, P., Gerbig, C., Rödenbeck, C., Karstens, U., Koch, T. F., and Heimann, M.: Atmospheric CO_2 inversions on the mesoscale using data-driven prior uncertainties: quantification of the European terrestrial CO_2 fluxes, Atmos. Chem. Phys., 18, 3047–3064, https://doi.org/10.5194/acp-18-3047-2018, 2018.

Kurosawa, K. and Poterjoy, J.: Data Assimilation Challenges Posed by Nonlinear Operators: A Comparative Study of Ensemble and Variational Filters and Smoothers, https://doi.org/10.1175/MWR-D-20-0368.1, 2021.

Lauvaux, T., Schuh, A. E., Bocquet, M., Wu, L., Richardson, S., Miles, N., and Davis, K. J.: Network design for mesoscale inversions of CO_2 sources and sinks, Tellus B: Chem. Phys. Meteorol., 64, 17980, https://doi.org/10.3402/tellusb.v64i0.17980, 2012.

Li, J. and Li, Y.: Ozone deterioration over North China plain caused by light absorption of black carbon and organic carbon, Atmos. Environ., 313, 120048, https://doi.org/10.1016/j.atmosenv.2023.120048, 2023.

Li, X., Hu, X.-M., Cai, C., Jia, Q., Zhang, Y., Liu, J., Xue, M., Xu, J., Wen, R., and Crowell, S. M. R.: Terrestrial CO_2 Fluxes, Concentrations, Sources and Budget in Northeast China: Observational and Modeling Studies, J. Geophys. Res.-Atmos., 125, https://doi.org/10.1029/2019jd031686, 2020.

Liu, J., Bowman, K. W., and Henze, D. K.: Source-receptor relationships of column-average CO_2 and implications for the impact of observations on flux inversions, J. Geophys. Res.-Atmos., 120, 5214–5236, https://doi.org/10.1002/2014JD022914, 2015.

Liu, J., Bowman, K. W., and Lee, M.: Comparison between the Local Ensemble Transform Kalman Filter (LETKF) and 4D-Var in atmospheric CO_2 flux inversion with the Goddard Earth Observing System-Chem model and the observation impact diagnostics from the LETKF, J. Geophys. Res.-Atmos., 121, 13066–13087, https://doi.org/10.1002/2016jd025100, 2016.

Ma, C., Wang, T., Mizzi, A. P., Anderson, J. L., Zhuang, B., Xie, M., and Wu, R.: Multiconstituent Data Assimilation With WRF-Chem/DART: Potential for Adjusting Anthropogenic Emissions and Improving Air Quality Forecasts Over Eastern China, J. Geophys. Res.-Atmos., 124, 7393–7412, https://doi.org/10.1029/2019jd030421, 2019.

Mahadevan, P., Wofsy, S. C., Matross, D. M., Xiao, X., Dunn, A. L., Lin, J. C., Gerbig, C., Munger, J. W., Chow, V. Y., and Gottlieb, E. W.: A satellite-based biosphere parameterization for net ecosystem CO_2 exchange: Vegetation Photosynthesis and Respiration Model (VPRM), Global Biogeochem. Cy., 22, https://doi.org/10.1029/2006gb002735, 2008.

Miyoshi, T., Kondo, K., and Imamura, T.: The 10,240-member ensemble Kalman filtering with an intermediate AGCM, Geophys. Res. Lett., 41, 5264–5271, https://doi.org/10.1002/2014gl060863, 2014.

Monteil, G., Broquet, G., Scholze, M., Lang, M., Karstens, U., Gerbig, C., Koch, F.-T., Smith, N. E., Thompson, R. L., Luijkx, I. T., White, E., Meesters, A., Ciais, P., Ganesan, A. L., Manning, A., Mischurow, M., Peters, W., Peylin, P., Tarniewicz, J., Rigby, M., Rödenbeck, C., Vermeulen, A., and Walton, E. M.: The regional European atmospheric transport inversion comparison, EUROCOM: first results on European-wide terrestrial carbon fluxes for the period 2006–2015, Atmos. Chem. Phys., 20, 12063–12091, https://doi.org/10.5194/acp-20-12063-2020, 2020.

Müller, S., Schüler, L., Zech, A., and Heße, F.: GSTools v1.3: a toolbox for geostatistical modelling in Python, Geosci. Model Dev., 15, 3161–3182, https://doi.org/10.5194/gmd-15-3161-2022, 2022.

Munassar, S., Monteil, G., Scholze, M., Karstens, U., Rödenbeck, C., Koch, F.-T., Totsche, K. U., and Gerbig, C.: Why do inverse models disagree? A case study with two European CO_2 inversions, Atmos. Chem. Phys., 23, 2813–2828, https://doi.org/10.5194/acp-23-2813-2023, 2023.

Niwa, Y., Tomita, H., Satoh, M., Imasu, R., Sawa, Y., Tsuboi, K., Matsueda, H., Machida, T., Sasakawa, M., Belan, B., and Saigusa, N.: A 4D-Var inversion system based on the icosahedral grid model (NICAM-TM 4D-Var v1.0) – Part 1: Offline forward and adjoint transport models, Geosci. Model Dev., 10, 1157–1174, https://doi.org/10.5194/gmd-10-1157-2017, 2017a.

Niwa, Y., Fujii, Y., Sawa, Y., Iida, Y., Ito, A., Satoh, M., Imasu, R., Tsuboi, K., Matsueda, H., and Saigusa, N.: A 4D-Var inversion system based on the icosahedral grid model (NICAM-TM 4D-Var v1.0) – Part 2: Optimization scheme and identical twin experiment of atmospheric CO_2 inversion, Geosci. Model Dev., 10, 2201–2219, https://doi.org/10.5194/gmd-10-2201-2017, 2017b.

Niwa, Y., Ishijima, K., Ito, A., and Iida, Y.: Toward a long-term atmospheric CO_2 inversion for elucidating natural carbon fluxes: technical notes of NISMON-CO_2 v2021.1, Prog. Earth Planet. Sci., 9, https://doi.org/10.1186/s40645-022-00502-6, 2022.

OCO-2/OCO-3 Science Team, Payne, V., and Chatterjee, A.: OCO-2 Level 2 bias-corrected XCO_2 and other select fields from the full-physics retrieval aggregated as daily files v11.0, Goddard Earth Sciences Data and Information Services Center (GES DISC) [data set], https://doi.org/10.5067/5Q8JLZL1VD4A, 2024.

Piao, S., He, Y., Wang, X., and Chen, F.: Estimation of China's terrestrial ecosystem carbon sink: Methods, progress and prospects, Sci. China Earth Sci., 65, 641–651, https://doi.org/10.1007/s11430-021-9892-6, 2022.

Pleim, J. E.: A Combined Local and Nonlocal Closure Model for the Atmospheric Boundary Layer. Part I: Model Description and Testing, J. Appl. Meteorol. Climatol., https://doi.org/10.1175/JAM2539.1, 2007.

Raju, A., Sijikumar, S., Burman, P. K. D., Valsala, V., Tiwari, Y. K., Mukherjee, S., Lohani, P., and Kumar, K.: Very high-resolution Net Ecosystem Exchange over India using Vegetation Photosynthesis and Respiration Model (VPRM) simulations, Ecol. Modell., 481, https://doi.org/10.1016/j.ecolmodel.2023.110340, 2023.

Rao, C. R.: Some Statistical Problems in Multitarget Tracking, in: Statistical Decision Theory and Related Topics V, 513–521, https://doi.org/10.1007/978-1-4612-2618-5_40, 1994.

Schuh, A. E., Byrne, B., Jacobson, A. R., Crowell, S. M. R., Deng, F., Baker, D. F., Johnson, M. S., Philip, S., and Weir, B.: On the role of atmospheric model transport uncertainty in estimating the Chinese land carbon sink, Nature, 603, E13–E14, https://doi.org/10.1038/s41586-021-04258-9, 2022.

Sengupta, D. and Jammalamadaka, S. R.: Linear models and regression with R: an integrated approach, second, World Scientific, https://doi.org/10.1142/11282, 2020.

Sotos, A. E. C., Vanhoof, S., Noortgate, W. V. D., and Onghena, P.: The transitivity misconception of Pearson's correlation coefficient, Stat. Educ. Res. J., 8, 33–55, https://doi.org/10.52041/serj.v8i2.394, 2009.

Storm, I., Karstens, U., D'Onofrio, C., Vermeulen, A., and Peters, W.: A view of the European carbon flux landscape through the lens of the ICOS atmospheric observation network, Atmos. Chem. Phys., 23, 4993–5008, https://doi.org/10.5194/acp-23-4993-2023, 2023.

Super, I., Denier van der Gon, H. A. C., van der Molen, M. K., Dellaert, S. N. C., and Peters, W.: Optimizing a dynamic fossil fuel CO_2 emission model with CTDAS (CarbonTracker Data Assimilation Shell, v1.0) for an urban area using atmospheric observations of CO_2, CO, NO_x, and SO_2, Geosci. Model Dev., 13, 2695–2721, https://doi.org/10.5194/gmd-13-2695-2020, 2020.

Tanizaki, H.: Nonlinear Filters, Springer, Berlin, Heidelberg, https://doi.org/10.1007/978-3-662-03223-7, 1996.

van der Laan-Luijkx, I. T., van der Velde, I. R., van der Veen, E., Tsuruta, A., Stanislawska, K., Babenhauserheide, A., Zhang, H. F., Liu, Y., He, W., Chen, H., Masarie, K. A., Krol, M. C., and Peters, W.: The CarbonTracker Data Assimilation Shell (CTDAS) v1.0: implementation and global carbon balance 2001–2015, Geosci. Model Dev., 10, 2785–2800, https://doi.org/10.5194/gmd-10-2785-2017, 2017.

Wang, J., Feng, L., Palmer, P. I., Liu, Y., Fang, S., Bosch, H., O'Dell, C. W., Tang, X., Yang, D., Liu, L., and Xia, C.: Large Chinese land carbon sink estimated from atmospheric carbon dioxide data, Nature, 586, 720-+, https://doi.org/10.1038/s41586-020-2849-9, 2020.

Wang, S., Cohen, J. B., Guan, L., Lu, L., Tiwari, P., and Qin, K.: Observationally constrained global NOx and CO emissions variability reveals sources which contribute significantly to CO−2 emissions, npj Clim. Atmos. Sci., 8, 87, https://doi.org/10.1038/s41612-025-00977-2, 2025.

Wang, Y., Wang, X., Wang, K., Chevallier, F., Zhu, D., Lian, J., He, Y., Tian, H., Li, J., Zhu, J., Jeong, S., and Canadell, J. G.: The size of the land carbon sink in China, Nature, 603, E7–E9, https://doi.org/10.1038/s41586-021-04255-y, 2022.

Wanninkhof, R.: Relationship between wind speed and gas exchange over the ocean revisited, Limnol. Oceanogr.-Methods, 12, 351–362, https://doi.org/10.4319/lom.2014.12.351, 2014.

Wesloh, D., Keller, K., Feng, S., Lauvaux, T., and Davis, K. J.: Temporal Error Correlations in a Terrestrial Carbon Cycle Model Derived by Comparison to Carbon Dioxide Eddy Covariance Flux Tower Measurements, J. Geophys. Res.-Biogeosci., 129, e2023JG007526, https://doi.org/10.1029/2023JG007526, 2024.

World Data Centre for Greenhouse Gases: Global Atmosphere Watch (GAW) program data portal, https://gaw.kishou.go.jp/user, last access: 4 September 2025.

Wu, L., Bocquet, M., Chevallier, F., Lauvaux, T., and Davis, K.: Hyperparameter estimation for uncertainty quantification in mesoscale carbon dioxide inversions, Tellus B: Chem. Phys. Meteorol., 65, 20894, https://doi.org/10.3402/tellusb.v65i0.20894, 2013.

Zhao, S., Russell, M. G., Hakami, A., Capps, S. L., Turner, M. D., Henze, D. K., Percell, P. B., Resler, J., Shen, H., Russell, A. G., Nenes, A., Pappin, A. J., Napelenok, S. L., Bash, J. O., Fahey, K. M., Carmichael, G. R., Stanier, C. O., and Chai, T.: A multiphase CMAQ version 5.0 adjoint, Geosci. Model Dev., 13, 2925–2944, https://doi.org/10.5194/gmd-13-2925-2020, 2020.